This is to certify that the

dissertation entitled

Electromagnetic Dissociation of ^{8}B and the Rate of the $^{7}Be(p,gamma)^{8}B$ Reaction in the Sun

presented by

Barry Samuel Davids

has been accepted towards fulfillment
of the requirements for

Ph.D degree in Physics

Major professor

Date 03 November 2000

ELECTROMAGNETIC DISSOCIATION OF ^{8}B AND THE RATE OF THE ^{7}Be(p,γ)^{8}B REACTION IN THE SUN

By

Barry Samuel Davids

A DISSERTATION

Submitted to
Michigan State University
in partial fulfillment of the requirements
for the Degree of

DOCTOR OF PHILOSOPHY

Department of Physics and Astronomy

2000

ABSTRACT

ELECTROMAGNETIC DISSOCIATION OF ^{8}B AND THE RATE OF THE ^{7}Be(p,γ)^{8}B REACTION IN THE SUN

By

Barry Samuel Davids

In an effort to better determine the ^{7}Be(p,γ)^{8}B reaction rate, we have performed inclusive and exclusive measurements of the Coulomb dissociation of ^{8}B. The former was a study of longitudinal momentum distributions of ^{7}Be fragments emitted in the Coulomb breakup of intermediate energy ^{8}B beams on Pb and Ag targets. Analysis of these data yielded the $E2$ contribution to the breakup cross section. In the exclusive measurement, we determined the cross section for the Coulomb breakup of ^{8}B on Pb at low relative energies in order to infer the astrophysical S factor for the ^{7}Be(p,γ)^{8}B reaction. Interpreting the measurements with 1st-order perturbation theory, we obtained $S_{E2}/S_{E1} = 4.7\ ^{+2.0}_{-1.3} \times 10^{-4}$ at $E_{rel} = 0.6$ MeV, and $S_{17}(0) = 17.8\ ^{+1.4}_{-1.2}$ eV b. Semiclassical 1st-order perturbation theory and fully quantum mechanical continuum-discretized coupled channels analyses yield nearly identical results for the E1 strength relevant to solar neutrino flux calculations, suggesting that theoretical reaction mechanism uncertainties need not limit the precision of Coulomb breakup determinations of the ^{7}Be(p,γ)^{8}B S factor. A recommended value of $S_{17}(0)$ based on a weighted average of this and other measurements is presented.

To my family

ACKNOWLEDGMENTS

I would like to express my deepest thanks to my principal collaborators, Sam M. Austin, Daniel Bazin, Henning Esbensen, and Brad Sherrill. Their knowledge, intelligence, experience, patience, and equanimity made this work possible.

Henning Esbensen did all of the perturbation theory calculations presented in this thesis that were not done by me, and the coupled channels calculations were carried out by Jeff Tostevin and Ian Thompson. Takashi Nakamura contributed prodigiously to the 2nd experiment.

Thanks go to all those who helped make these experiments successful: Don Anthony, Tom Aumann, Thomas Baumann, Bertram Blank, Jac Caggiano, Marielle Chartier, Ryan Clement, Cary Davids, Patrick Hui, Pat Lofy, Chris Powell, Heiko Scheit, Mathias Steiner, Peter Thirolf, John Yurkon, Al Zeller, and the staff of the NSCL.

CONTENTS

LIST OF TABLES

LIST OF FIGURES

Chapter 1

Introduction

The Sun is a source of energy upon which all life on Earth relies. The origin of this energy was a mystery until the late 1930s, when discoveries in nuclear physics made it possible for Hans Bethe to suggest that a series of thermonuclear reactions fusing hydrogen into helium caused the sun to shine. Nearly 30 years elapsed before this hypothesis was supported by the detection of neutrinos produced in these nuclear reactions here on Earth. The light created deep in the solar interior follows a tortuous path, scattering many times before emerging from the surface some 10 million years after it was produced. For this reason, it carries little information about the center of the Sun. On the other hand, the neutrinos copiously produced in the nuclear reactions powering the Sun stream outward freely, rarely interacting with the matter in the solar interior. By detecting these neutrinos on Earth, we directly probe conditions deep in the Sun.

As shown in Fig. 1.1, the flux of neutrinos emanating from the solar interior consists predominantly of low energy electron neutrinos from the $p + p \rightarrow d + e^+ + \nu_e$ reaction [1]. The higher energy ^{8}B neutrinos, though they constitute less than 10^{-4} of the total solar neutrino flux, are the best studied. Their flux, direction, and energy spectrum have been measured in large chlorine radiochemical and water

Cerenkov detectors. Less than half the number of ^{8}B neutrinos expected on the basis of standard solar models and standard electroweak particle physics has been observed in terrestrial detectors [2], a situation that has come to be known as the ^{8}B solar neutrino problem. This discrepancy between theory and experiment appears to be resolved best by invoking oscillations of ν_e into other neutrino flavors. By measuring the ratio of charged current to neutral current interactions, the heavy water detector SNO will stringently test neutrino oscillation hypotheses. In order to calculate the theoretical solar neutrino flux and interpret the results of measurements at SNO and other neutrino detectors, the rate of the radiative capture reaction that produces ^{8}B in the Sun, ^{7}Be(p,γ)^{8}B, must be known to a precision of 5% [1]. Thus astrophysics, nuclear physics, and particle physics meet in addressing the solar neutrino problem.

The cross section for the ^{7}Be(p,γ)^{8}B reaction has been measured directly in several experiments [3, 4, 5, 6, 7, 8, 9]. Although the shape of the excitation function is well determined, there is a large spread in the absolute normalizations of these measurements. The cross section must be known at the very low relative energies ($\sim$ 20 keV) relevant to ^{8}B production in the Sun, but these low energies are experimentally inaccessible because the high Coulomb barrier causes the cross section to plummet with decreasing energy. The strategy adopted is to measure the cross section at the lowest possible energy, and then extrapolate downward using theory. In order to extrapolate to low energies reliably, the dominant energy dependences in the cross section can be factored out, leaving a quantity known as the astrophysical S factor, which varies much more slowly with energy. The S factor is defined by

$$S(E) \;=\; E\;\sigma(E)\;exp[2\pi Z_1 Z_2 e^2/(\hbar v)], \tag{1.1}$$

where the Z_i are the charges, v the relative velocity, and E the center-of-mass energy of the nuclei involved. Conventionally, the value of the S factor for the ^{7}Be(p,γ)^{8}B reaction, S_{17}, is extrapolated from the data at accessible energies to zero energy.

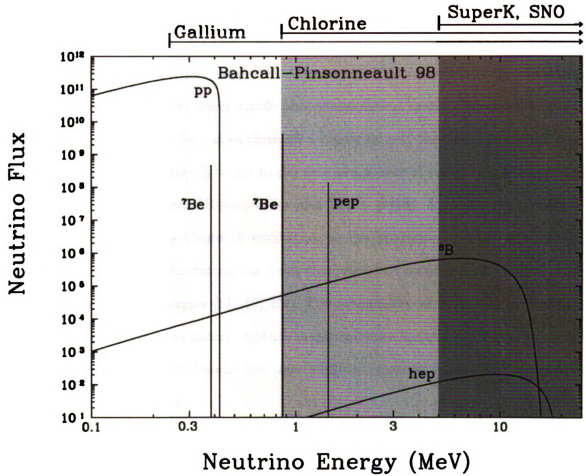

Figure 1.1: Fluxes of neutrinos ($cm^{-2}\ s^{-1}$) produced by different nuclear reactions in the Sun predicted by the standard solar model of ref. [1]. The energy ranges in which several neutrino detectors are sensitive are shown on the top of the figure.

In light of the disagreements among the radiative capture measurements of the ^{7}Be(p,γ)^{8}B cross section, and the fact that direct measurements at very low energies are impractical, indirect techniques have been developed to infer this radiative capture cross section. Such techniques are subject to different systematic uncertainties. For photons of a given multipolarity, the detailed balance theorem relates the cross section for radiative capture to that for the corresponding inverse reaction, photodissociation. In the case of the ^{7}Be(p,γ)^{8}B reaction, the ^{8}B nucleus is radioactive with a half life of 770 ms and is not a viable photodissociation target. However, when an energetic beam of ^{8}B nuclei passes through a heavy target, the time-dependent electromagnetic field of the high Z target nuclei acts as a source of virtual photons capable of dissociating the incident ^{8}B projectiles into ^{7}Be + p [10]. This process, known as Coulomb dissociation, is Coulomb excitation to the continuum. The semiclassical formalism of Coulomb excitation has been extended to Coulomb dissociation at intermediate and high energies [11, 12, 13]. The advantages of high energy Coulomb dissociation over direct radiative capture measurements include thicker targets and larger cross sections, and thereby the possibility of reaching lower relative energies with an appreciable yield.

Coulomb dissociation has been used to infer $S_{17}(0)$ [14, 15, 16], but the method is not without complications. First, several electromagnetic multipoles contribute in Coulomb dissociation, e.g., $E1$, $E2$, and $M1$, while the radiative capture reaction is mainly driven by a single electromagnetic multipole transition at solar energies, $E1$. Second, even though the electromagnetic interaction dominates, the effects of nuclear absorption and diffraction must be considered. Finally, one must consider the effects of higher-order electromagnetic transitions that can destroy the simple correspondence between radiative capture and Coulomb dissociation. An important experimental challenge is to identify and understand these complications in order

to firmly establish Coulomb dissociation as a viable alternative to direct radiative capture measurements. In this thesis, I will show that these complications can be dealt with in a satisfactory manner by a judicious choice of the experimental conditions and by applying tested nuclear structure and reaction theories.

The first challenge, that of disentangling the contributions of different electromagnetic multipoles to extract one in particular, can be met by carefully studying the angular distribution of the breakup fragments. In the Coulomb dissociation of intermediate energy ^{8}B, $E2$ is the principal unwanted electromagnetic multipole. By carrying out an inclusive measurement of the ^{7}Be fragments emitted in the Coulomb dissociation of 44 and 81 MeV/nucleon ^{8}B, we determined the $E2$ contribution to the breakup cross section.

Having measured the $E2$ strength in the Coulomb breakup, we were in a position to study the breakup energy spectrum, $d\sigma/dE_{rel}$, in order to determine the $E1$ strength at low relative energies and thereby infer $S_{17}(0)$. This was done in a exclusive measurement with an 83 MeV/nucleon ^{8}B beam. In the analysis of this experiment, we used the $E2$ strength determined in the inclusive measurement, and investigated the influence of nuclear and higher-order electromagnetic processes. We discovered that these complications could be minimized, and the theoretical uncertainties made small enough that our Coulomb breakup measurement is of comparable precision to the direct radiative capture measurements. In this thesis, I shall describe the inclusive and exclusive measurements, and interpret them using both 1st-order perturbation theory and a continuum-discretized coupled channels approach. Finally I will compare the inferred value of $S_{17}(0)$ with recent direct and indirect measurements.

Chapter 2

Experimental Procedures

2.1 Inclusive Measurements

We bombarded a 1.9 g cm^{-2} Be production target with 100 and 125 MeV/nucleon ^{12}C beams from the K1200 cyclotron at the National Superconducting Cyclotron Laboratory (NSCL). Typical ^{12}C beam intensities were 10-50 pnA. Fragmentation reactions in the Be target yielded secondary beams of 44 and 81 MeV/nucleon ^{8}B, after magnetic analysis in the A1200 fragment separator [17]. A 200 mg cm^{-2} $(CH_2)_n$ achromatic energy degrader aided in the purification of the secondary beams. Slits limited the momentum spread of the secondary beams to $\pm$ 0.25%. A 17 mg cm^{-2} plastic scintillator just downstream of the A1200 focal plane provided time-of-flight and secondary beam intensity information. Typical ^{8}B beam intensities ranged from (4-20) $\times$ 10^3 s^{-1}. Table 2.1 shows the total number of ^{8}B nuclei that struck each target.

The ^{8}B beams were transported through a second beam analysis line to the target position of the S800 spectrometer, as shown schematically in Fig. 2.1. This analysis line dispersed the secondary beams according to their momenta, resulting in a 5 cm $\times$ 1 cm beam spot on the targets. A ladder held 27 mg cm^{-2} Ag and 28 mg cm^{-2} Pb

Table 2.1: Total number of ^{8}B nuclei on target

Target	Beam Energy (MeV/nucleon)	^{8}B on Target (10^6)
Ag	44	360
Ag	81	1 070
Pb	44	840
Pb	81	2 980

targets. A 300 μm Si *p-i-n* diode detector mounted on a ladder 18 cm upstream of the targets was intermittently raised into the path of the beam. Energy loss signals from this detector, in conjunction with timing signals from the plastic scintillator at the exit of the A1200, yielded both the transmission and composition of the secondary beams. Times-of-flight were measured for the $\sim$ 70 m flight path between the scintillator at the exit of the A1200 and the S800 focal plane. Fig. 2.2 shows a typical plot of the signals in the *p-i-n* diode detector versus time-of-flight.

The secondary beams were not monoisotopic; ^{7}Be was the principal contaminant, and was 5-8 times more intense than the ^{8}B component of the beam. Two other nuclei, ^{6}Li and ^{9}C, were also present in the beam. As the energies of these contaminants differed substantially from that of the ^{8}B ions, their different times-of-flight provided reliable particle identification.

We used the S800 spectrometer [18] to detect the ^{7}Be fragments emitted in the Coulomb dissociation of ^{8}B nuclei on the Ag and Pb targets. The spectrometer was set at 0°, and was operated in a dispersion-matched energy loss mode so that the 0.5% spread in the momentum of the ^{8}B beams did not limit the final momentum resolution, which was dominated by differential energy loss in the target. The large

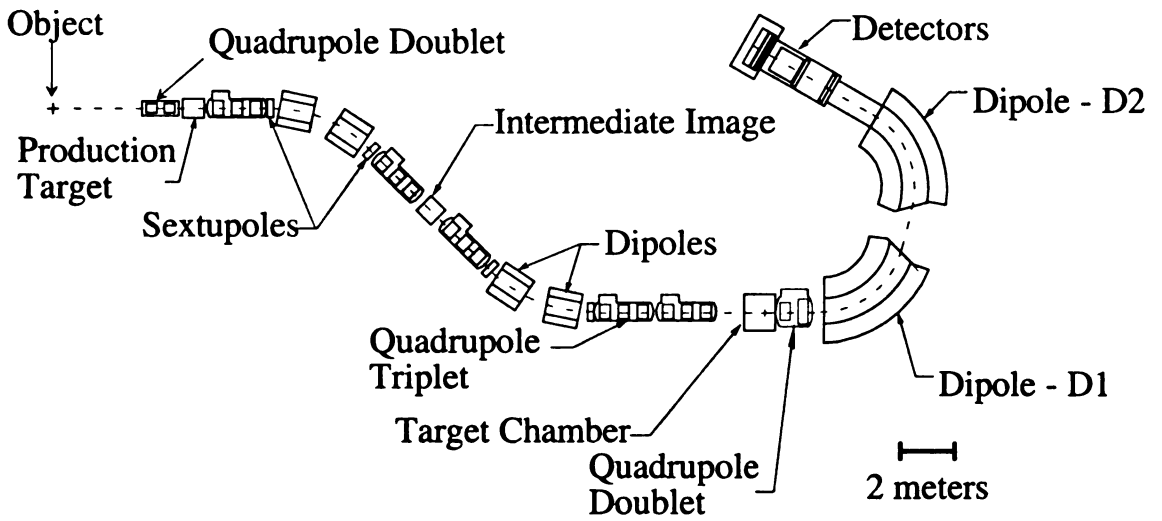

Figure 2.1: Schematic view of the S800 spectrometer at the NSCL.

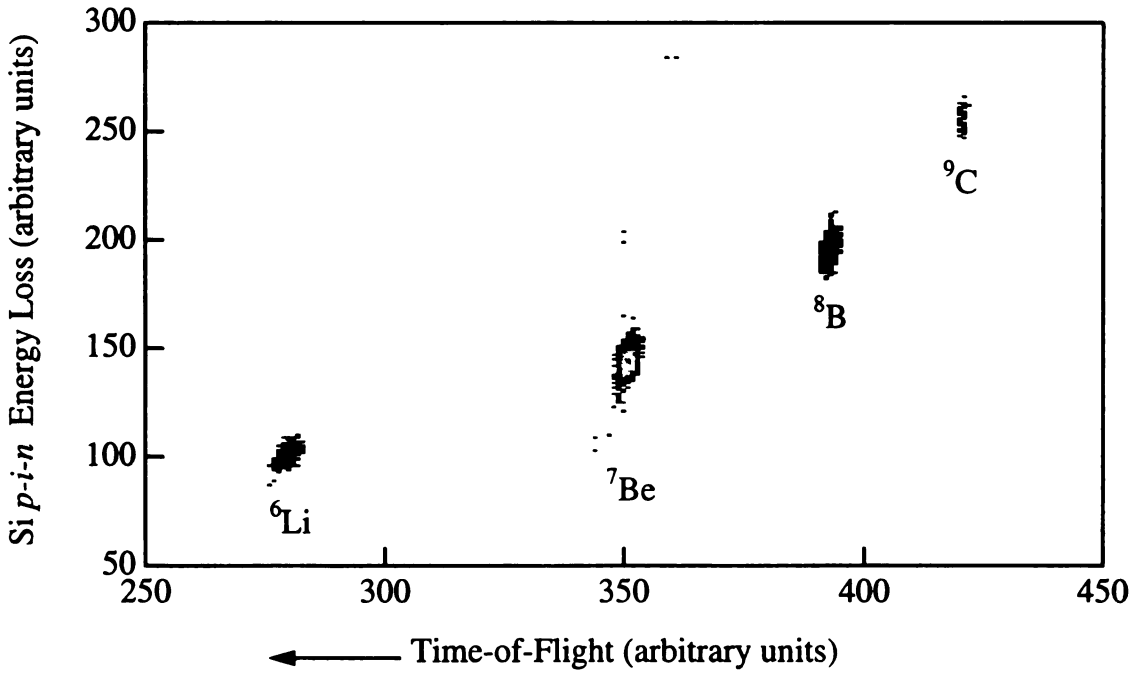

Figure 2.2: Typical Si *p-i-n* diode versus time-of-flight spectrum illustrating the secondary beam composition.

angular acceptance (20 msr) and momentum acceptance (6%) of the S800 allowed us to capture essentially the entire momentum distribution at a single magnetic field setting.

The standard complement of detectors at the focal plane of the S800 spectrometer comprises two position-sensitive cathode readout drift chambers (CRDCs), a 41 cm deep, 16 segment ionization chamber, and three plastic scintillators. The CRDCs are separated by 1 meter to give good angular resolution. Ref. [19] describes these detectors in detail. The ionization chamber recorded the energy losses, and the first, 5 cm thick scintillator measured the total energies of particles reaching the focal plane. This information was sufficient to identify the ^{7}Be breakup fragments unambiguously, as illustrated in Fig. 2.3; the time-of-flight data provided a check. As the nuclei of interest were stopped in the first scintillator, the other two were not used. The particle identification was confirmed through comparisons with calibration beams of ^{7}Be that had the same magnetic rigidity as the ^{8}B beams. The higher magnetic rigidity of the detected ^{7}Be fragments compared to the ^{8}B beams made the focal plane particle identification particularly clean.

The positions and angles of the ^{7}Be fragments were measured in the CRDCs. The position resolution obtained was approximately 0.3 mm (1σ), yielding an intrinsic angular resolution of about 2 mrad. We employed the ion optics code COSY INFINITY [20] to reconstruct the trajectories of the ^{7}Be fragments from their measured positions in the CRDCs, and the magnetic fields of the spectrometer, which were continuously monitored by nuclear magnetic resonance probes throughout the experiment. We calculated the ^{7}Be lab momenta and scattering angles on an event-by-event basis, allowing reconstruction of the longitudinal momentum distributions.

Corrections to the momentum distributions were made for two different effects. First, the overall efficiency of the CRDCs was less than unity due to a high threshold

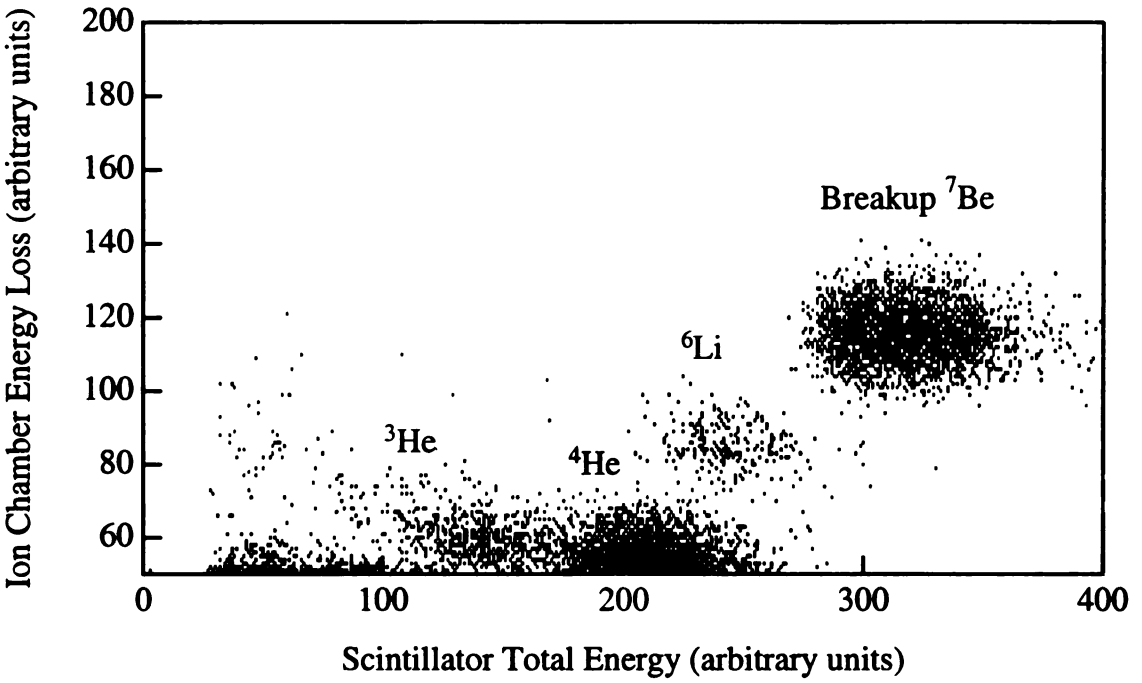

Figure 2.3: Typical ionization chamber energy loss versus stopping scintillator total energy spectrum.

on the anode wire constant fraction discriminator. This was a small correction in the case of the low energy beam (< 3%), but larger for the high energy beam (< 15%). The second was a momentum-dependent correction for the angular acceptance of the S800, which was important for events having large deviations from the central momentum and large projections of the scattering angle in the dispersive direction of the spectrometer. These corrections affected only the tails of the measured momentum distributions, and amounted to less than 5% of the measured cross sections, even for the largest scattering angles. Corrections were made on the basis of the data themselves by observations of the acceptance limits. Uncertainties equal to half the size of the corrections were assigned to the data points in the momentum distributions that required correction. During some runs, the magnetic field of the spectrometer was varied to move the center of the distribution away from the center of the focal plane detectors in order to measure the tails of the momentum distributions precisely. The

final momentum distributions represent the sums of measurements made at several different magnetic field settings.

2.2 Exclusive Measurement

The 83 MeV/nucleon ^{8}B beam used in the exclusive measurement was produced with a 125 MeV/nucleon primary ^{12}C beam in the same manner described above. Typical ^{8}B beam intensities were 10^{4} s^{-1}, and the momentum spread in the beam was limited to $\pm$ 0.25% by slits in the A1200 fragment separator. A total of 4×10^{9} ^{8}B nuclei were incident on the target. A thin plastic scintillator was placed at the exit of the A1200 fragment separator for beam intensity, transmission, and time-of-flight measurements. The ^{8}B nuclei were dissociated in a 47 mg cm^{-2} Pb target located in front of a room temperature 1.5 T dipole magnet. Four position-sensitive multiwire drift chambers (MWDCs) [21] recorded the positions of the ^{7}Be and p fragments produced in the breakup after they passed through the magnetic field. Two MWDCs measured each breakup fragment, allowing the determination of both position and angle. A 16 element array of 4 cm thick plastic scintillator bars was placed behind the MWDCs. A 25 mm $\times$ 60 mm stainless steel plate located directly in front of the first ^{7}Be MWDC absorbed nearly all of the direct beam. The composition of the secondary beam in the exclusive measurement was roughly 20% ^{6}Li, 55% ^{7}Be, 20% ^{8}B, and 5% ^{9}C. Fig. 2.4 shows a schematic drawing of the experimental setup.

The multiwire drift chambers used in this experiment have active areas of 112 mm $\times$ 112 mm, and use delay-line readout to measure the positions of particle tracks. The chambers were filled with P30 (70% argon, 30% methane) at a pressure of 700 torr. Each MWDC has two orthogonal wire planes, providing both x and y positions. The positions are deduced as follows. The signals from time-to-digital converters connected to each end of the delay line are subtracted, yielding a spectrum such as

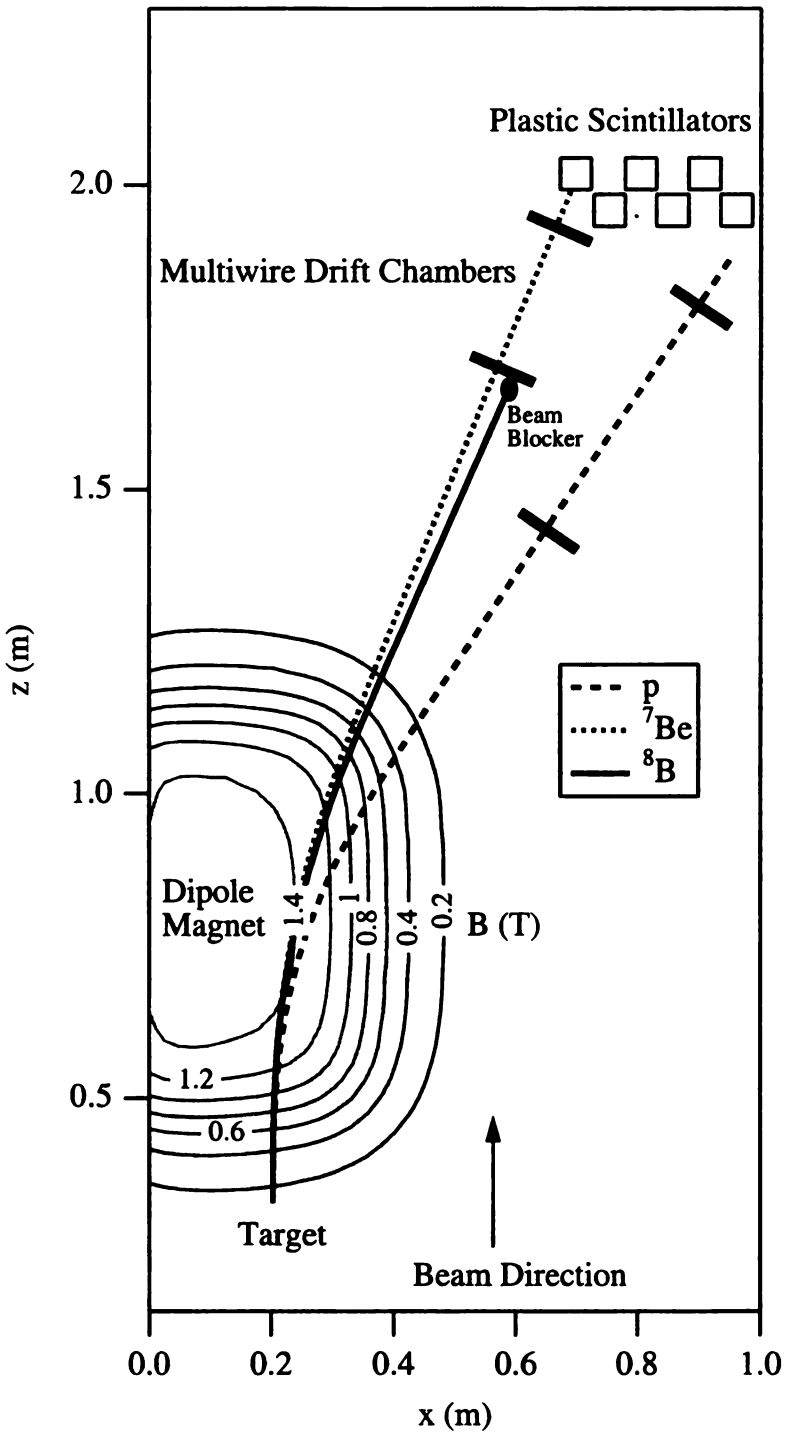

Figure 2.4: Schematic view of the experimental setup for the exclusive measurement showing the detectors, typical trajectories, and contours of constant magnetic field produced by the dipole magnet.

that shown in Fig. 2.5. The peaks in this spectrum correspond to individual anode wires, which are separated by 8 mm. Drift time information is used to interpolate between anode wires using current pulses induced on the cathode field-shaping wires. The drift time is obtained from the sum of the delay line time signals; an example of such a spectrum is shown in Fig. 2.6. This spectrum does not show a uniform distribution of drift times. By integrating such spectra with respect to time and fitting the result with a polynomial, one obtains calibrated curves of drift distance as a function of drift time. These time signals do not reveal on which side of an anode wire an ion passed. The charge collected on the cathode field-shaping wires resolves this ambiguity. Alternate cathode wires are bussed together, so that ions nearer to the left side of anode wires produce larger signals in one set of cathode wires than in the other. Fig. 2.7 depicts a typical spectrum of the signals from one set of cathode wires versus the signals from the other set. All of the ions passing on the left of an anode wire are in one group, and those passing on the right fall in the other group. The principles of operation and geometry of these detectors are described in detail in ref. [21]. Position resolutions of 0.4 mm (1σ) were obtained for protons and ^{7}Be fragments.

Particle identification was achieved through measurements of energy loss in the plastic scintillator array and time-of-flight between the exit of the A1200 and the scintillator array. The geometric average of signals from photomultiplier tubes on the top and bottom of each scintillator bar served as a measure of particle energy loss. Since the scintillator array was not sufficiently thick to stop the breakup fragments, direct total energy measurements were not possible, and the time-of-flight measurement was crucial for ion identification. Calibration beams of ^{7}Be and p having the same magnetic rigidity as the ^{8}B beam were used to confirm the particle identification. The protons and ^{7}Be struck widely separated scintillator bars, allowing optimization

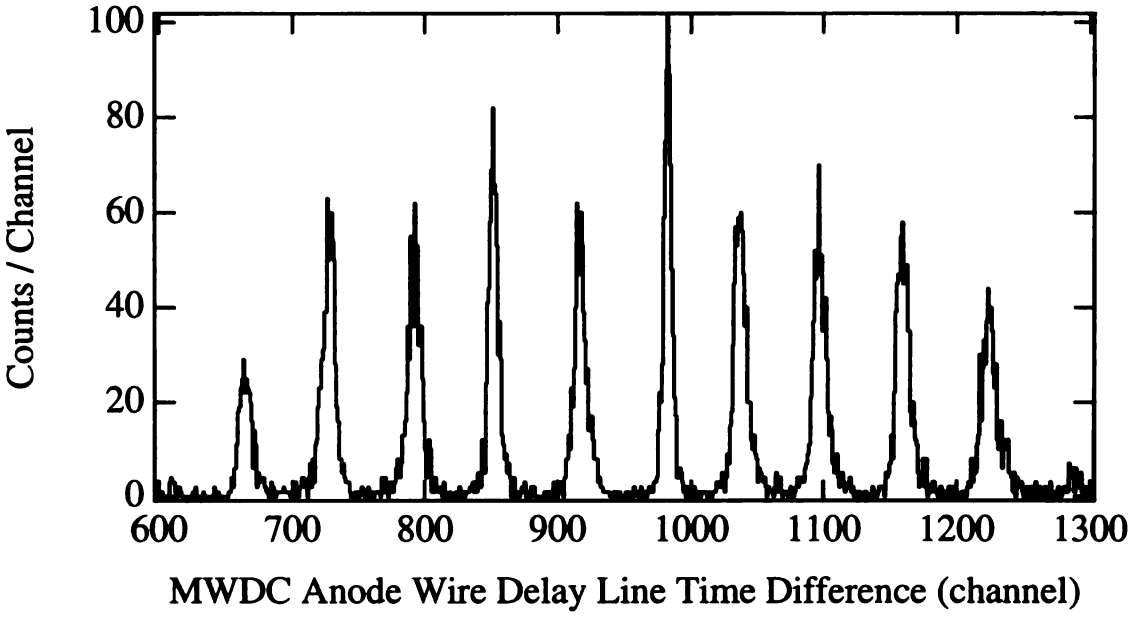

Figure 2.5: Spectrum of the differences between the times for voltage pulses to reach each end of the delay line in a MWDC. Individual wire peaks are plainly visible.

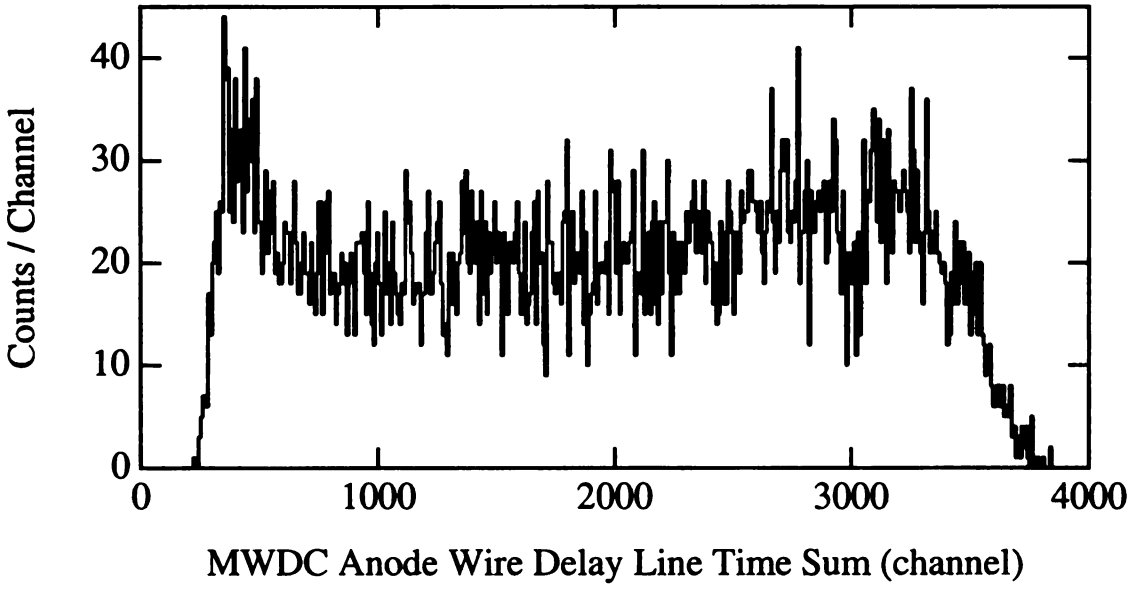

Figure 2.6: Spectrum of the sums of the times for voltage pulses induced by electron clouds to reach each end of the delay line in a MWDC. The maximum drift time corresponds to a distance of 4 mm.

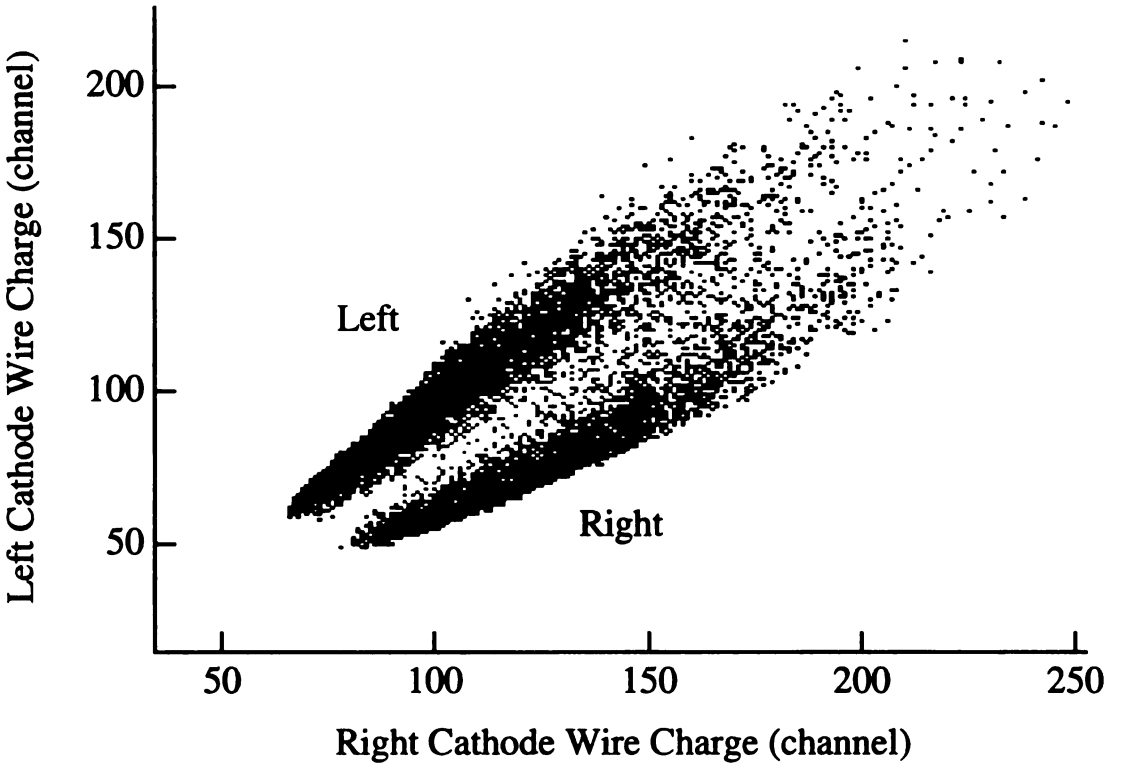

Figure 2.7: Spectrum of the signals from one set of MWDC cathode field-shaping wires versus those from the other set. The two groups correspond to ions passing on the left of a given anode wire and ions passing on the right.

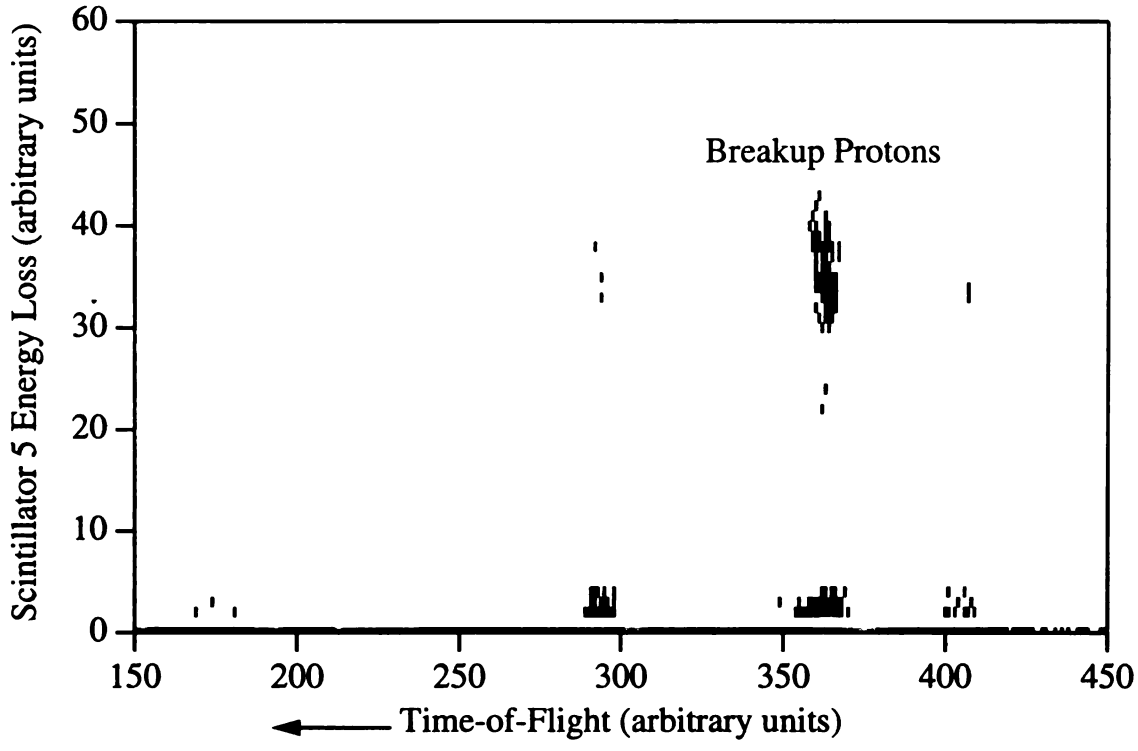

Figure 2.8: Typical proton scintillator bar energy loss versus time-of-flight spectrum. The events with small scintillator signals represent crosstalk from adjacent scintillator bars.

of the individual bar electronics for the appropriate fragment energy losses. Fig. 2.8 shows the scintillator energy loss versus time-of-flight spectrum for a scintillator bar that detected protons, while Fig. 2.9 shows that for a bar used to detect ^{7}Be fragments. These spectra are gated, requiring a good position signal in at least one proton MWDC plane and one ^{7}Be MWDC plane.

We reconstructed the 4-momenta of the breakup fragments from the measured positions in all 8 MWDC planes and the magnetic field using the ion optics code COSY INFINITY [22]. The magnetic field was measured with a Hall probe at 2184 points in each of 4 planes in the gap of the dipole magnet to a precision of $\pm$ 2 mG [23]. Second-order Taylor series expansions about a reference trajectory were employed, and the trajectory reconstruction was checked through the use of proton

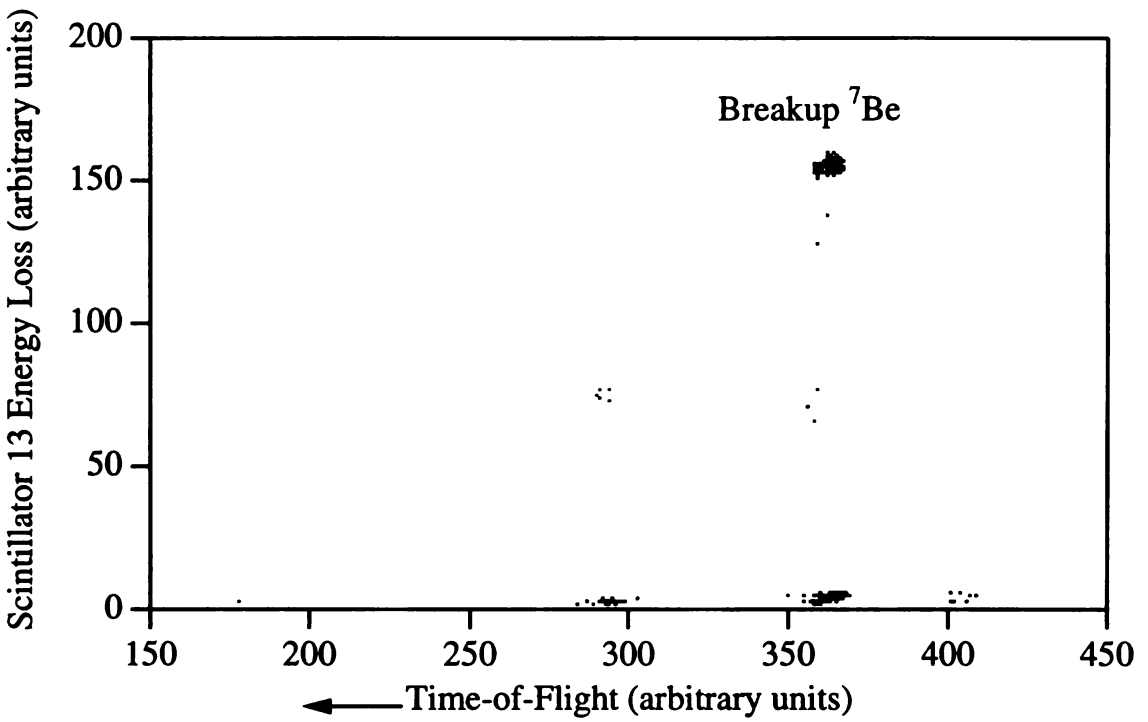

Figure 2.9: Typical ^{7}Be scintillator bar energy loss versus time-of-flight spectrum. The events with small scintillator signals are due to light produced in adjacent scintillator bars.

and ^{7}Be calibration beams. The invariant mass method was used to calculate the relative energy of the fragments according to

$$E_{rel} = \sqrt{E^2 - \mathbf{p}^2} - m_{Be}c^2 - m_p c^2, \tag{2.1}$$

where E is the total relativistic energy, and $\mathbf{p}$ the total momentum in the laboratory frame. The energy and momentum are defined by

$$E = \gamma_{Be} m_{Be} c^2 + \gamma_p m_p c^2, \tag{2.2}$$

and

$$\mathbf{p} = \gamma_{Be} m_{Be} \mathbf{v}_{Be} + \gamma_p m_p \mathbf{v}_p. \tag{2.3}$$

The relative energy is simply the kinetic energy in the center-of-mass reference frame. We obtained a relative energy resolution of 55 keV (1σ) at $E_{rel} = 100$ keV; the energy resolution increased for higher relative energies approximately as $\sqrt{E_{rel}}$. The small separation between the 1st and 2nd MWDCs, combined with the MWDC position resolution, caused the angular resolution to limit the relative energy resolution. This small distance was necessitated by the requirement that the first detector be far enough away from the magnet that there be adequate separation between the ^{7}Be fragments and the ^{8}B beam, and by the limitations of an existing vacuum chamber. Other contributions to the relative energy resolution included energy loss and multiple scattering in the 47 mg cm^{-2} target and the MWDCs, each of which was 30 mg cm^{-2} thick.

The resolution and efficiency of the experimental apparatus were determined through a Monte Carlo simulation. The inputs to the simulation included the beam emittance (6 mm beam spot diameter, $\pm$ 6 mrad in the dispersive direction of the magnet, $\pm$ 9 mrad in the non-dispersive direction) and the measured detector position resolution. The beam emittance was measured by reducing the magnetic field, causing the ^{8}B beam to miss the beam blocker and be detected in the MWDCs, while the

detector position resolution was determined through the use of a mask. The Monte Carlo simulation was also used to calculate the small fraction of the ^{7}Be breakup fragments that were intercepted by the beam blocker. The FORTRAN source code of the Monte Carlo simulation is available at http://www.nscl.msu.edu/~sherrill/davids.

In order to evaluate the geometric efficiency of the setup, we employed a model for the breakup of ^{8}B that includes both $E1$ and $E2$ transition amplitudes, which have different distributions in $\Theta_{^8B}$, the laboratory scattering angle of the excited ^{8}B. To account for the $E1$-$E2$ interference observed in the asymmetry of the longitudinal momentum distribution of ^{7}Be fragments, we included an anisotropic angular distribution of the breakup fragments in the excited ^{8}B rest frame. The shape of this distribution is similar to those shown in Fig. 9 of ref. [24], but was empirically adjusted to reproduce the longitudinal momentum distribution of protons measured in this experiment, which will be discussed in section 3.1. The $E1$ and $E2$ dissociation probabilities were taken from the model of ref. [24], after scaling the $E2$ matrix elements by the factor 0.7. This quenching of the $E2$ amplitudes, required for the best fit of the inclusive data, is discussed in more detail below. We gauged the model-dependence of the efficiency determination by also computing the efficiency using the same model without $E2$ transitions. The difference between the computed efficiencies with and without $E2$ transitions was less than 5% for the angular and relative energy ranges covered in the experiment. This difference was used as the theoretical uncertainty in the efficiency determination.

Since both $E2$ transitions and nuclear absorption and diffraction effects are relatively more important at small impact parameters than at large ones, we imposed a impact parameter cutoff at 30 fm. For 83 MeV/nucleon ^{8}B on Pb, this corresponds classically to $\Theta_{^8B} = 1.77°$. In practice, $\Theta_{^8B}$ was determined from the reconstructed total laboratory momentum vector, and the 1σ resolution of this quantity was 4.5

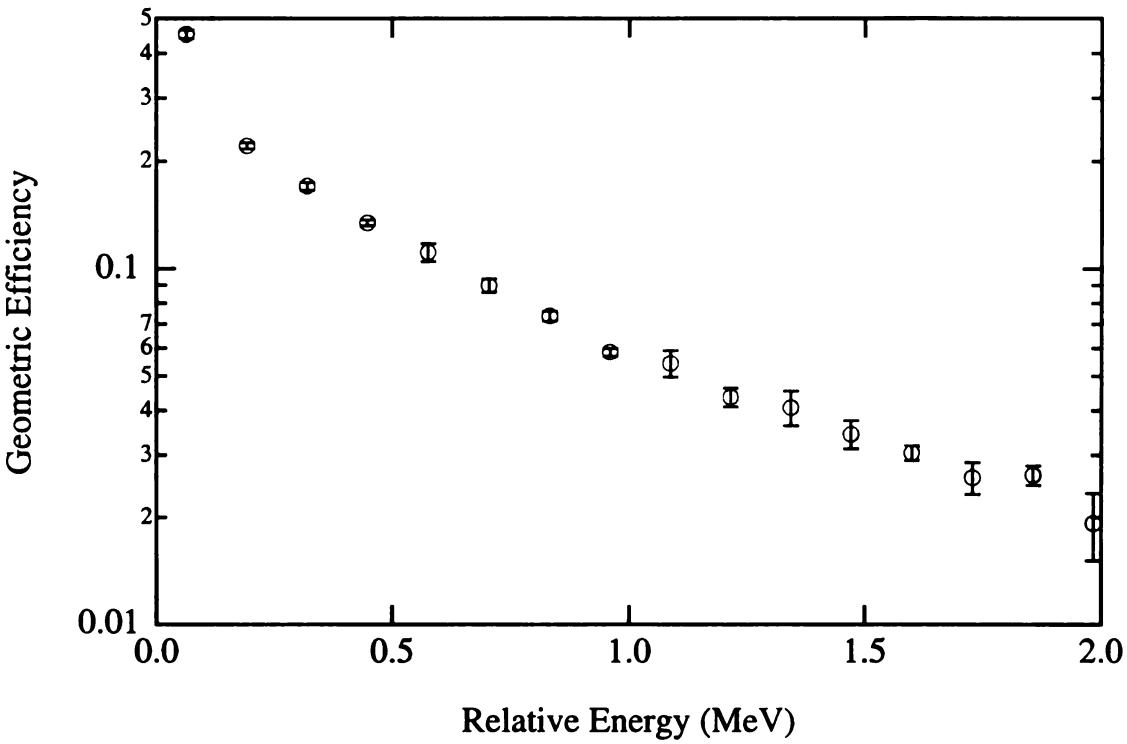

Figure 2.10: Geometric efficiency for detecting protons and ^{7}Be fragments in coincidence from the Coulomb dissociation of 83 MeV/nucleon ^{8}B with impact parameters $\geq$ 30 fm. The relative errors shown are statistical uncertainties from the simulation and theoretical uncertainties from the size of the $E2$ component, added in quadrature.

mrad. The geometric efficiency for detecting ^{8}B breakups with b $\geq$ 30 fm is shown in Fig. 2.10. The efficiency falls off rapidly with increasing relative energy, primarily due to the small solid angle subtended by the proton MWDCs. As the goal of the experiment was to determine the Coulomb dissociation cross section at low relative energies, the experimental arrangement was most sensitive to the events of interest. The intrinsic detection efficiency, i.e., the probability that all 8 MWDC planes provided good position signals when the breakup fragments passed through them, was measured to be 0.414 $\pm$ 0.008 using the scintillator array.

Chapter 3

Experimental Results and Analysis

3.1 Longitudinal Momentum Distributions

Measured laboratory frame longitudinal momentum distributions of ^{7}Be fragments from the Coulomb breakup of 44 MeV/nucleon ^{8}B on a Pb target are shown in Fig. 3.1. The momentum resolution obtained was 5 MeV/c, and the error bars indicate the relative uncertainties of the data points, which are dominated by statistical errors. The systematic uncertainty in the measured cross section due to target thickness and beam intensity was $\pm$ 9%. This systematic uncertainty is common to all of the ^{7}Be momentum distribution measurements. Fig. 3.1 also includes the results of 1st-order perturbation theory calculations performed using a modified version of the model of ref. [24]. Both the overall normalization and the $E2$ matrix elements of this calculation have been scaled, the former by 1.22 and the latter by 0.7. We shall return to this point later.

To investigate any possible dependence of higher-order electromagnetic effects on target charge, we also made inclusive measurements with an Ag target. The measured longitudinal momentum distributions of ^{7}Be fragments produced in the dissociation of 44 MeV/nucleon ^{8}B on Ag are shown in Fig. 3.2 for several different maximum

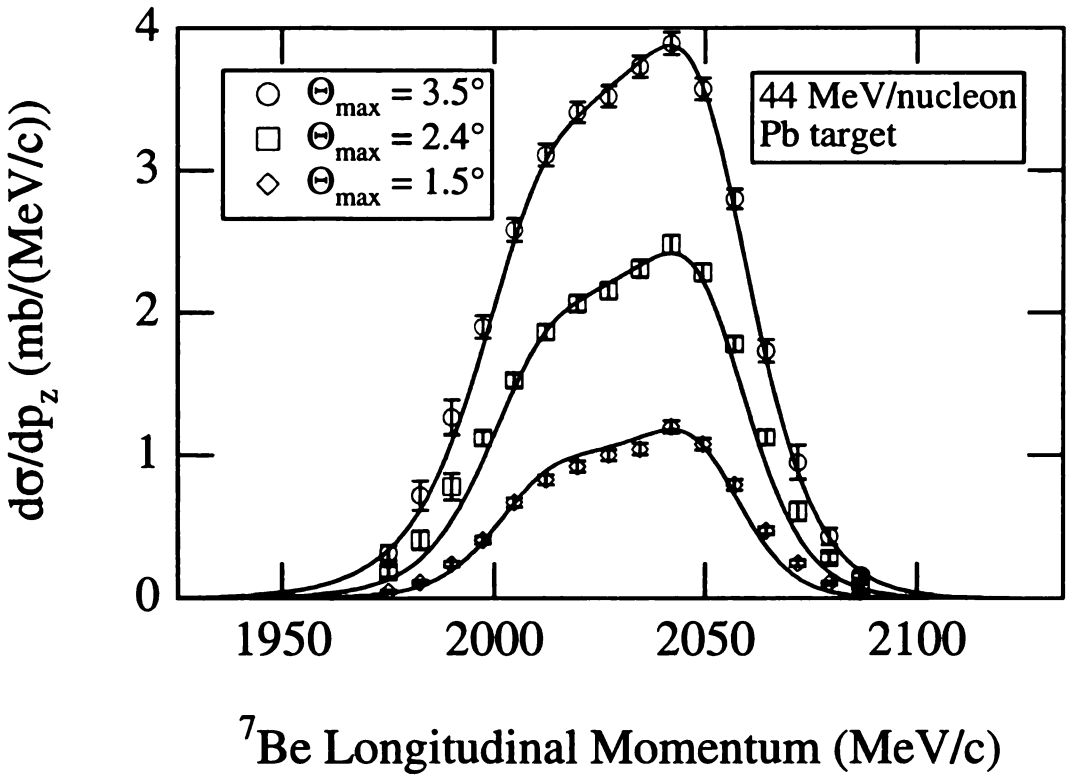

Figure 3.1: Measured longitudinal momentum distributions of ^{7}Be fragments from the Coulomb dissociation of 44 MeV/nucleon ^{8}B on Pb with several maximum ^{7}Be scattering angle cuts. Also shown are 1st-order perturbation theory calculations convoluted with the experimental resolution. See the text for details.

^{7}Be scattering angle cuts. The agreement with the 1st-order perturbation theory calculations done with the model of ref. [24] (shown here only for $\Theta_{max} = 1.5°$) is not as good as it is with the Pb target. In particular, the magnitude and width of the calculations are insufficient to describe the data. Suspecting that nuclear processes not accounted for in the Coulomb dissociation calculation were responsible for this discord, we simulated a nuclear contribution to the breakup momentum distribution with a gaussian distribution having a width (σ) of 35 MeV/c. This parametrization was motivated by the measurement of ref. [25] of the nuclear-induced breakup of 41 MeV/nucleon ^{8}B on a Be target. Arbitrarily scaling the normalization of the gaussian, we added this simulated nuclear contribution to 1st-order perturbation theory calculations having the same $E2$ matrix element scaling and overall normalization as the 44 MeV/nucleon Pb target calculations in order to minimize χ^2 for the central 6 points of the momentum distributions. The resulting curves are shown in Fig. 3.2. The point of this exercise was not to extract the nuclear-induced breakup component, but simply to see if the data could be described by such an incoherent sum of nuclear and Coulomb components. The agreement between these calculations and the measurements is fairly good. The difference between the Coulomb dissociation calculations and the data increased with maximum scattering angle, consistent with an increasing relative importance of nuclear-induced breakup. The breakup of ^{8}B on Ag can be studied with the CDCC method, but these results are outside the scope of this thesis, and will be presented elsewhere.

Placing different cuts on the angles of the emitted ^{7}Be fragments allows one to probe different impact parameters. However, a maximum ^{7}Be scattering angle does not correspond to a fixed minimum impact parameter, because the breakup energy and the angle of the emitted proton are not determined in the inclusive measurement. The sensitivities of the various angular cuts of the 44 MeV/nucleon longitudinal mo-

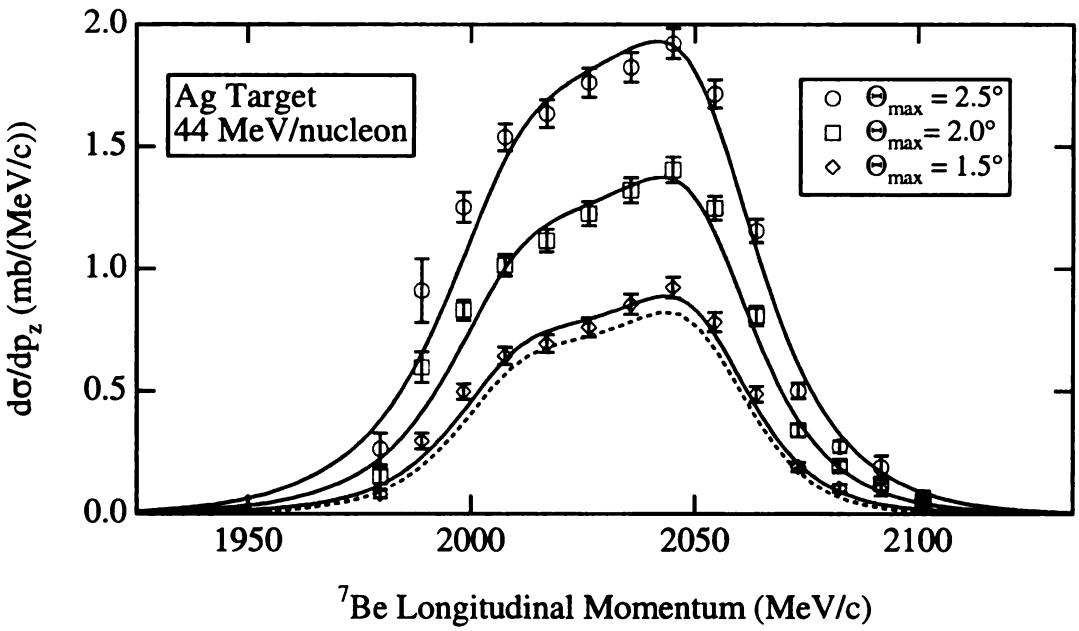

Figure 3.2: Laboratory frame longitudinal momentum distributions of ^{7}Be fragments with maximum scattering angles of 2.5°, 2.0°, and 1.5° emitted in the Coulomb dissociation of 44 MeV/nucleon ^{8}B on Ag. The solid curves represent an incoherent sum of the perturbative Coulomb dissociation calculations and a nuclear component simulated by a gaussian distribution (σ = 35 MeV/c). The dashed curve is the perturbative Coulomb dissociation calculation for the smallest angle cut.

mentum distributions to different impact parameters are shown in Fig. 3.3 for the Pb target and Fig. 3.4 for the Ag target. These curves are a measure of the relative probability that ^{7}Be fragments emitted in Coulomb breakups at various impact parameters will fall within specified angular cuts. The corresponding relative detection probability distributions as a function of impact parameter for the 81 MeV/nucleon beam are shown in Fig. 3.5 and Fig. 3.6. All of these calculations were performed using the model of ref. [24], with the $E2$ matrix elements scaled by 0.7 [26]. A comparison of the figures reveals that the Ag distributions probe smaller impact parameters than the Pb distributions, indicating that nuclear absorption and diffraction should play a larger role for the Ag target.

Fig. 3.7 shows the ^{7}Be longitudinal momentum distribution for the 81 MeV/nucleon ^{8}B beam on Ag with a maximum ^{7}Be scattering angle cut of 1.25°. The curve is a 1st-order perturbation theory calculation done with the model of ref. [24] with $E2$ matrix elements scaled by 0.7. The overall normalization of this calculation has not been altered. The perturbative calculation describes the data fairly well, with the most important discrepancy being the greater width of the measured distribution. It is possible that nuclear absorption and diffraction not accounted for in the Coulomb dissociation calculation broaden the measured distribution beyond the predicted extent.

The inclusive ^{7}Be longitudinal momentum distributions measured at 81 MeV/nucleon with the Pb target are depicted in Fig. 3.8 for ^{7}Be scattering angle cuts of 2.5°, 2.0°, and 1.5°. Also shown here are CDCC calculations convoluted with the experimental resolution of 5 MeV/c. The CDCC calculations describe the data reasonably well, accurately reproducing the slopes of the central regions of the momentum distributions, particularly for the largest angle cut. These calculations are not fits, but rather are absolute predictions based on the assumed structure model; the $E1$ and $E2$ ma-

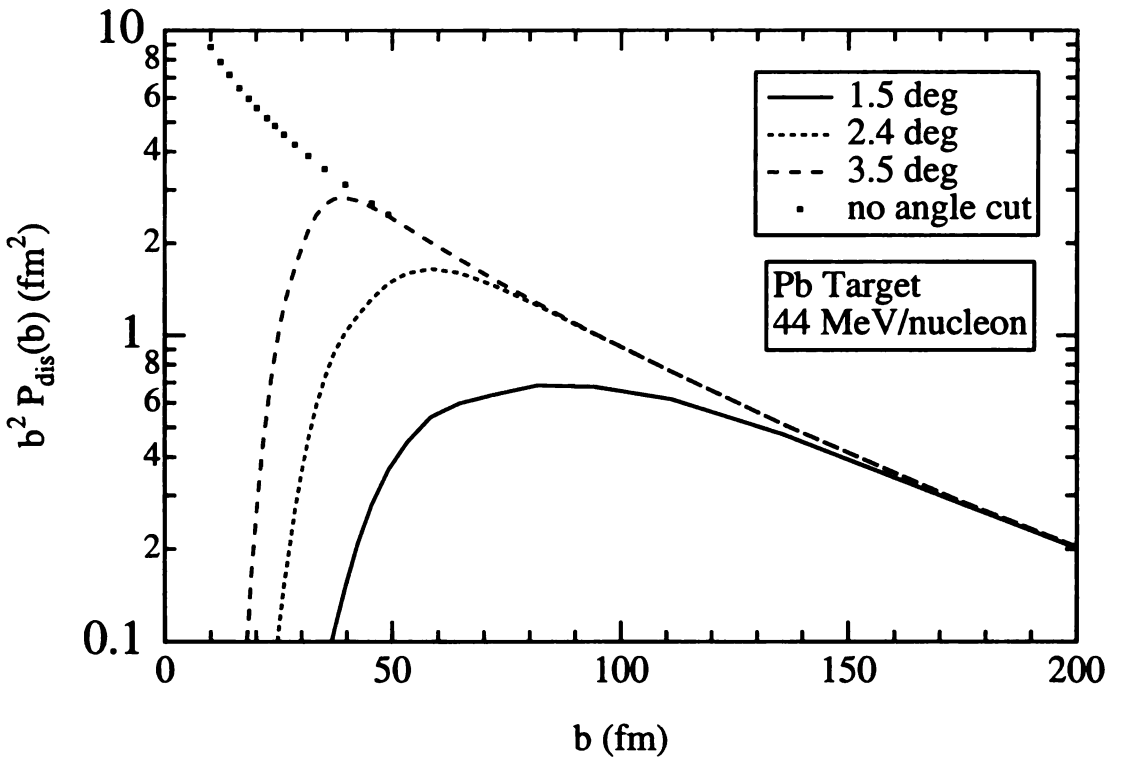

Figure 3.3: Product of Coulomb dissociation probability and impact parameter squared for the breakup of 44 MeV/nucleon ^{8}B on Pb with several maximum ^{7}Be scattering angle cuts as a function of impact parameter. This is a measure of the relative ^{7}Be detection probability, revealing the impact parameter sensitivity of the various angle cuts.

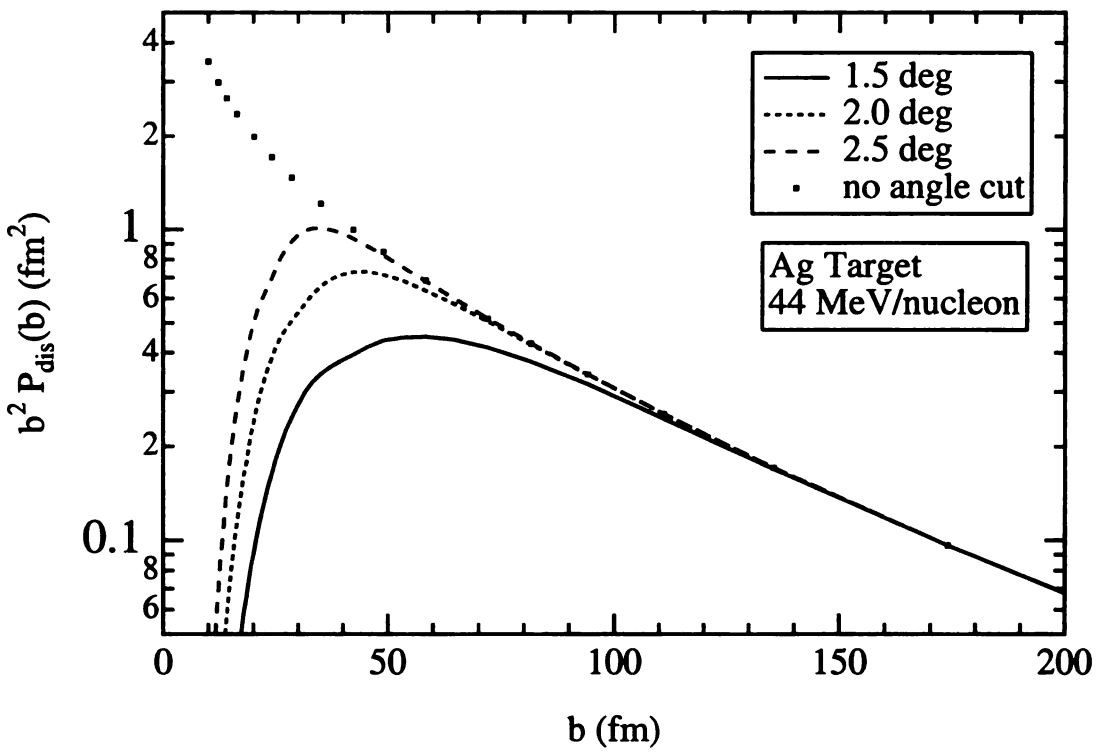

Figure 3.4: Product of Coulomb dissociation probability and impact parameter squared for the Coulomb dissociation of 44 MeV/nucleon ^{8}B on Ag for several maximum ^{7}Be scattering angle cuts as a function of impact parameter. This is a measure of the relative ^{7}Be detection probability, revealing the impact parameter sensitivity of the various angle cuts.

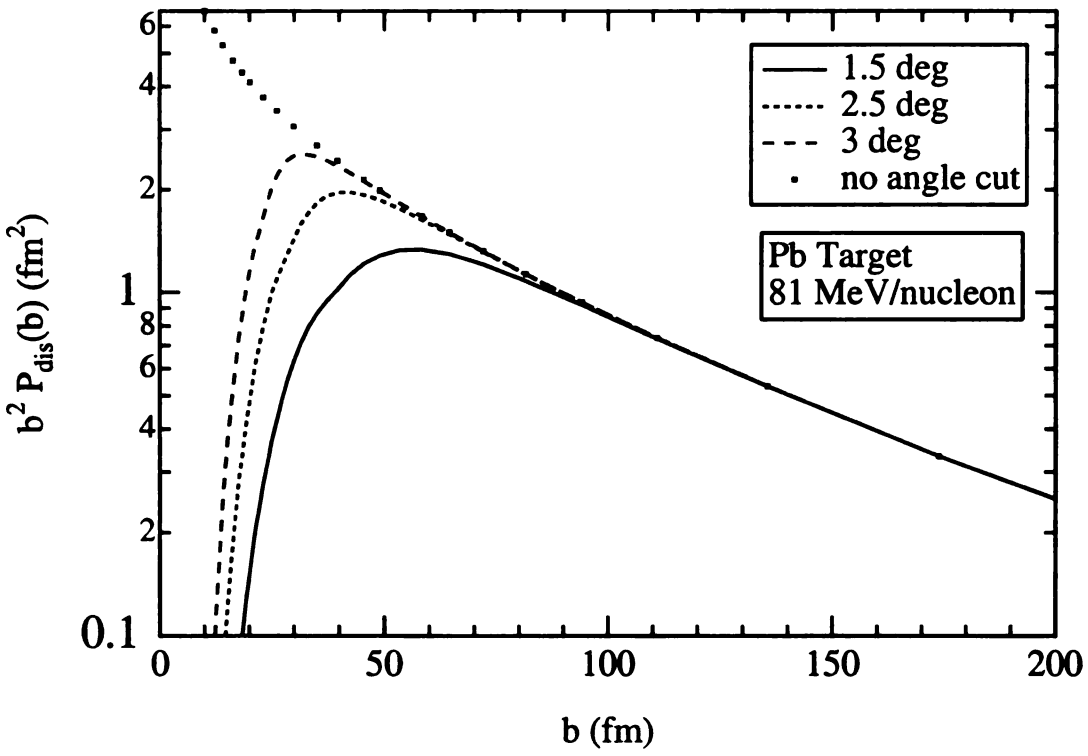

Figure 3.5: Product of Coulomb dissociation probability and impact parameter squared for the Coulomb breakup of 81 MeV/nucleon ^{8}B on Pb with several maximum scattering angle cuts as a function of impact parameter. This is a measure of the relative ^{7}Be detection probability, revealing the impact parameter sensitivity of the various angle cuts.

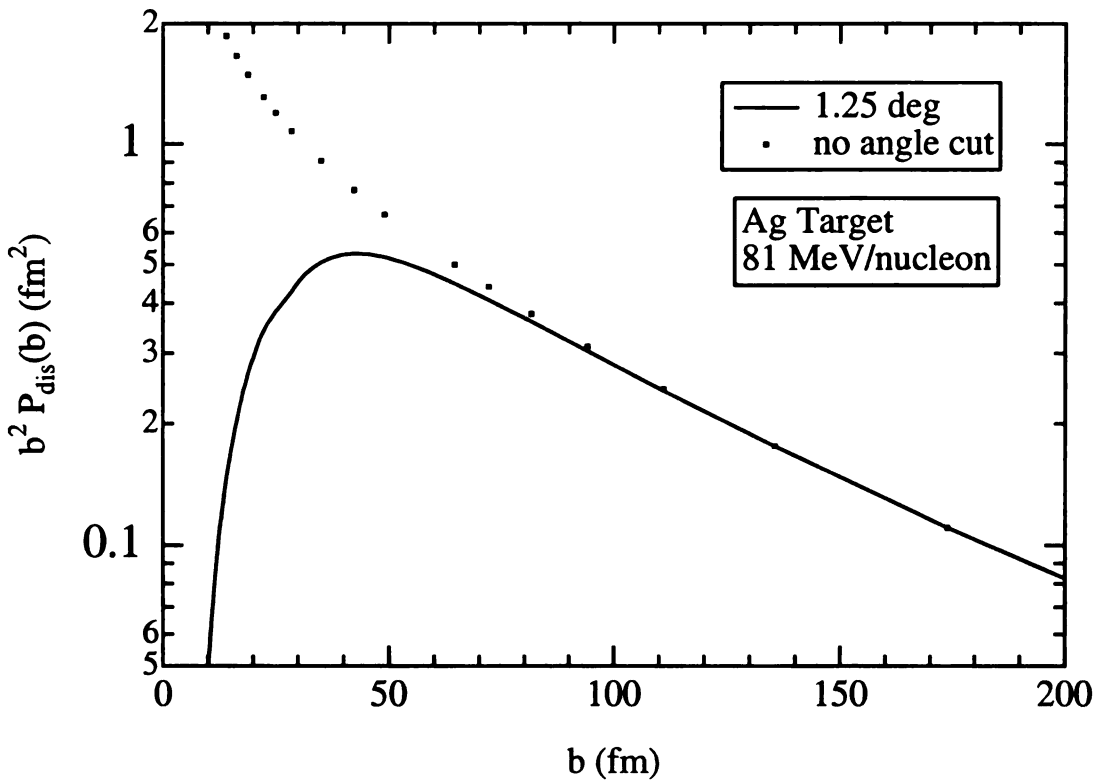

Figure 3.6: Product of Coulomb dissociation probability and impact parameter squared for the Coulomb dissociation of 81 MeV/nucleon ^{8}B on Ag with ^{7}Be scattering angles $\leq 1.25°$ as a function of impact parameter. This is a measure of the relative ^{7}Be detection probability, revealing the impact parameter sensitivity of this angle cut.

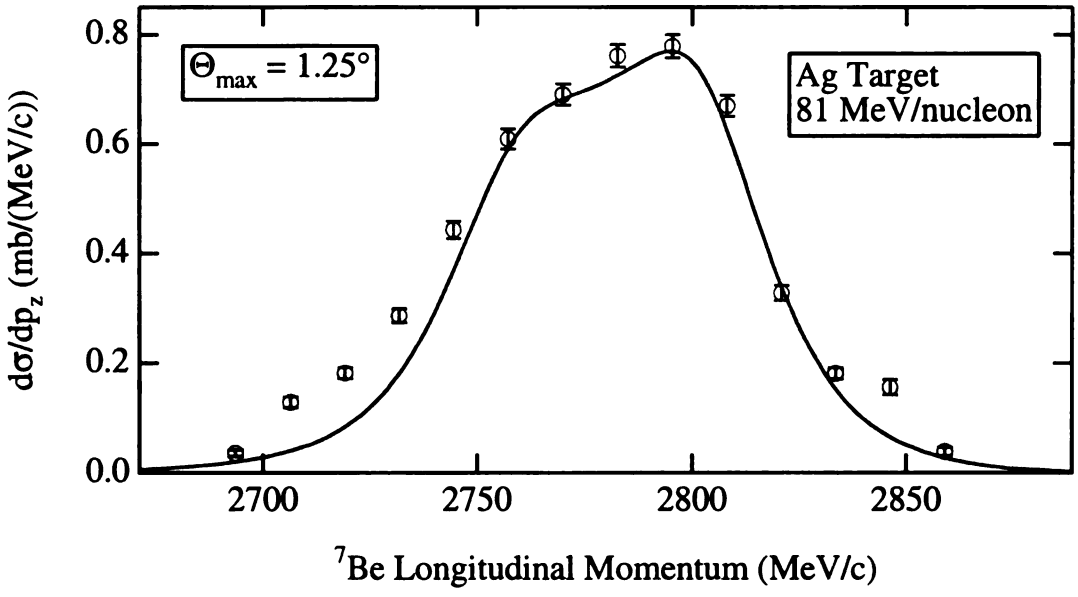

Figure 3.7: Laboratory frame longitudinal momentum distribution of ^{7}Be fragments with maximum scattering angles of 1.25° emitted in the Coulomb dissociation of 81 MeV/nucleon ^{8}B on Ag. The curve is a 1st-order perturbation theory calculation convoluted with the experimental resolution.

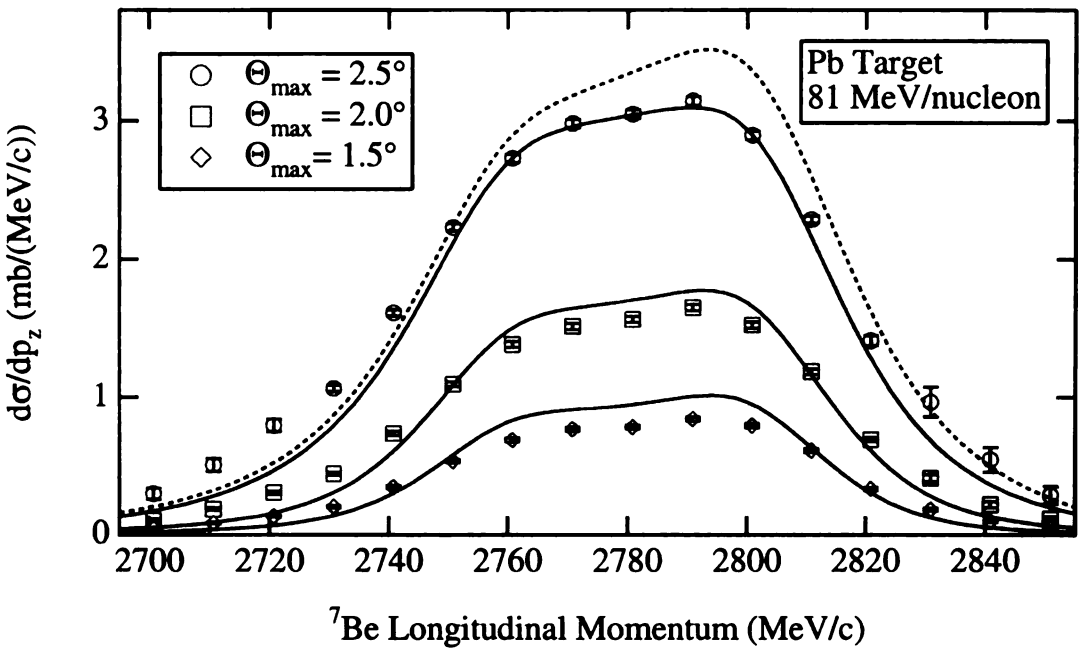

Figure 3.8: Laboratory frame longitudinal momentum distribution of ^{7}Be fragments emitted in the Coulomb dissociation of 81 MeV/nucleon ^{8}B on Pb with maximum scattering angles of 2.5°, 1.5°, and 1°. The solid curves are continuum-discretized coupled channels calculations that include both Coulomb and nuclear interactions, convoluted with the experimental resolution. The dashed curve is a DWBA calculation for $\Theta_{max} = 2.5°$.

trix elements have not been scaled in the CDCC calculations. The dashed curve is a distorted wave Born approximation (DWBA) calculation for the largest angle cut that assumes the same structure model and interactions as the CDCC calculation. The difference between the 1st-order DWBA and the CDCC calculations reflects the influence of higher-order processes, which tend to reduce the effective $E2$ strength needed in the 1st-order calculation. As is the case for the 81 MeV/nucleon Ag data, the calculations predict distributions narrower than were measured. The difference in magnitude between the calculations and the data for the smaller angle cuts is within the error due to the angular uncertainty of 0.25°.

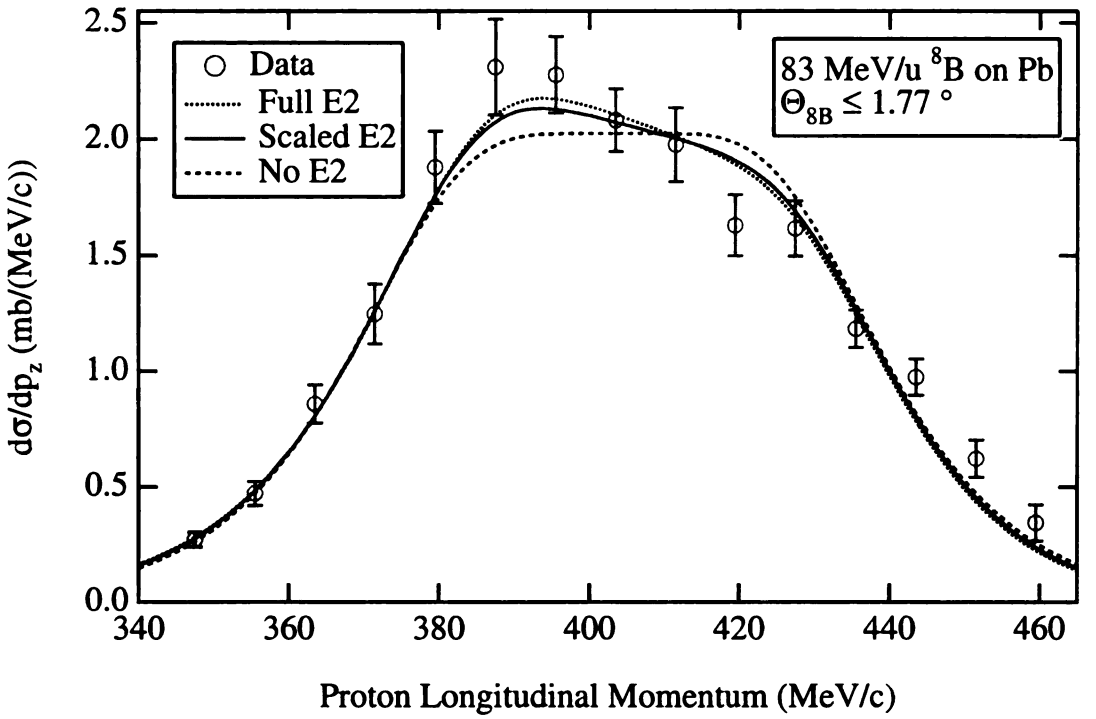

Figure 3.9: Measured longitudinal momentum distribution of protons from the Coulomb dissociation of 83 MeV/nucleon ^{8}B on Pb with ^{8}B scattering angles $\leq 1.77°$. Only relative errors are shown. Also depicted are 1st-order perturbation theory calculations with different E2 strengths, convoluted with the experimental resolution.

Fig. 3.9 depicts the longitudinal momentum distribution of protons measured in coincidence with ^{7}Be fragments from the Coulomb breakup of 83 MeV/nucleon ^{8}B with reconstructed ^{8}B center-of-mass angles of 1.77° and less. The proton momentum resolution was estimated from the Monte Carlo simulation to be 4 MeV/c (1σ). Also shown in the figure are 1st-order perturbation theory calculations using the model of ref. [24], one with the full $E2$ amplitude, one with the $E2$ matrix elements scaled by 0.7, and another with no $E2$ matrix elements. The overall normalization of the full $E2$ calculation was 0.90, while the calculation with scaled $E2$ matrix elements was multiplied by 0.95, and the calculation without $E2$ matrix elements was not scaled.

All of the measured longitudinal momentum distributions share a common feature:

an asymmetry attributed to interference between $E1$ and $E2$ transition amplitudes in the Coulomb breakup. This effect was first predicted in ref. [27]. An early measurement of the momentum distribution of ^{7}Be fragments from the Coulomb breakup of 41 MeV/nucleon ^{8}B on gold [25] provided evidence of this effect, but the statistics were insufficient to draw any definitive conclusions. By measuring longitudinal momentum distributions of ^{7}Be nuclei and protons on two targets at two different beam energies with two different experimental setups, we have conclusively demonstrated the existence of this asymmetry.

In 1st-order perturbation theory, the size of the predicted asymmetry is proportional to the $E2$ transition amplitude. Fig. 3.10 illustrates this point, depicting the central region of the 3.5° 44 MeV/nucleon ^{7}Be longitudinal momentum distribution from the Pb target along with three calculations. These calculations were performed with different $E2$ amplitudes, and are normalized to the same value at the center of the distribution. The simple potential model of ^{8}B structure from ref. [24] makes predictions for the $E1$ and $E2$ matrix elements. By arbitrarily scaling the $E1$ and $E2$ matrix elements in a 1st-order perturbation theory of the Coulomb breakup, we fit the central 6 data points of the 3.5° ^{7}Be longitudinal momentum distribution from the breakup of 44 MeV/nucleon ^{8}B on the Pb target in order to minimize the χ^2 value. Using this procedure, we found that the optimal ratio of $E2$ and $E1$ matrix element scaling factors was 0.7. The same ratio of matrix element scaling factors was required to best fit the 81 MeV/nucleon ^{7}Be longitudinal momentum distribution on Pb in perturbation theory, a calculation that is not shown here (see ref. [28]). In the exclusive experiment, it was not possible to measure the longitudinal momentum distributions with a precision comparable to that of the inclusive measurement. Furthermore, any nuclear-induced breakup contribution is relatively more important for the Ag target than for the Pb target. For these reasons, we used only the inclusive

measurements on Pb to deduce the $E2$ strength. The preliminary findings of the inclusive measurement were described previously [28]. In ref. [28], the optimal ratio of the $E2$ and $E1$ matrix element scaling factors was incorrectly reported as the ratio of the scaling factors for the $E2$ and $E1$ strength distributions; the correct value for this ratio is $0.7^2 = 0.49$. As a consequence, the reported [28] ratio of $E2$ and $E1$ S factors at $E_{rel} = 0.6$ MeV should be replaced by $4.7\ ^{+2.0}_{-1.3} \times 10^{-4}$. This result assumes the validity of 1st-order perturbation theory in describing the reaction mechanism, and a particular ^{8}B structure model. If higher-order electromagnetic effects are important, a larger intrinsic $E2$ strength is required to fit the data. Hence we have determined the effective $E2$ matrix element which, within a 1st-order perturbation theory with a given $E1$ matrix element, fits the empirically observed asymmetry in the longitudinal momentum distributions.

Table 3.1 lists the integrated cross sections obtained in the inclusive longitudinal momentum distribution measurements on both targets. The purpose of these inclusive measurements was to deduce the $E2$ strength in the Coulomb breakup. A determination of low-lying $E1$ strength would be subject to large nuclear structure uncertainties, since the inclusive measurements are sensitive to electromagnetic strength over a large range of excitation energies. However, the observed asymmetry in the longitudinal momentum distributions is a clear signature of $E1$-$E2$ interference, through which these measurements probe the total $E2$ strength.

3.2 Theoretical Methods

We have performed 1st-order perturbation theory calculations of the Coulomb dissociation of ^{8}B using the model of ref. [24], and have used them to interpret both the inclusive and exclusive measurements. This simple, single-particle potential model describes ^{8}B as a $p_{3/2}$ proton coupled to an inert $3/2^-$ ^{7}Be core. The model predicts

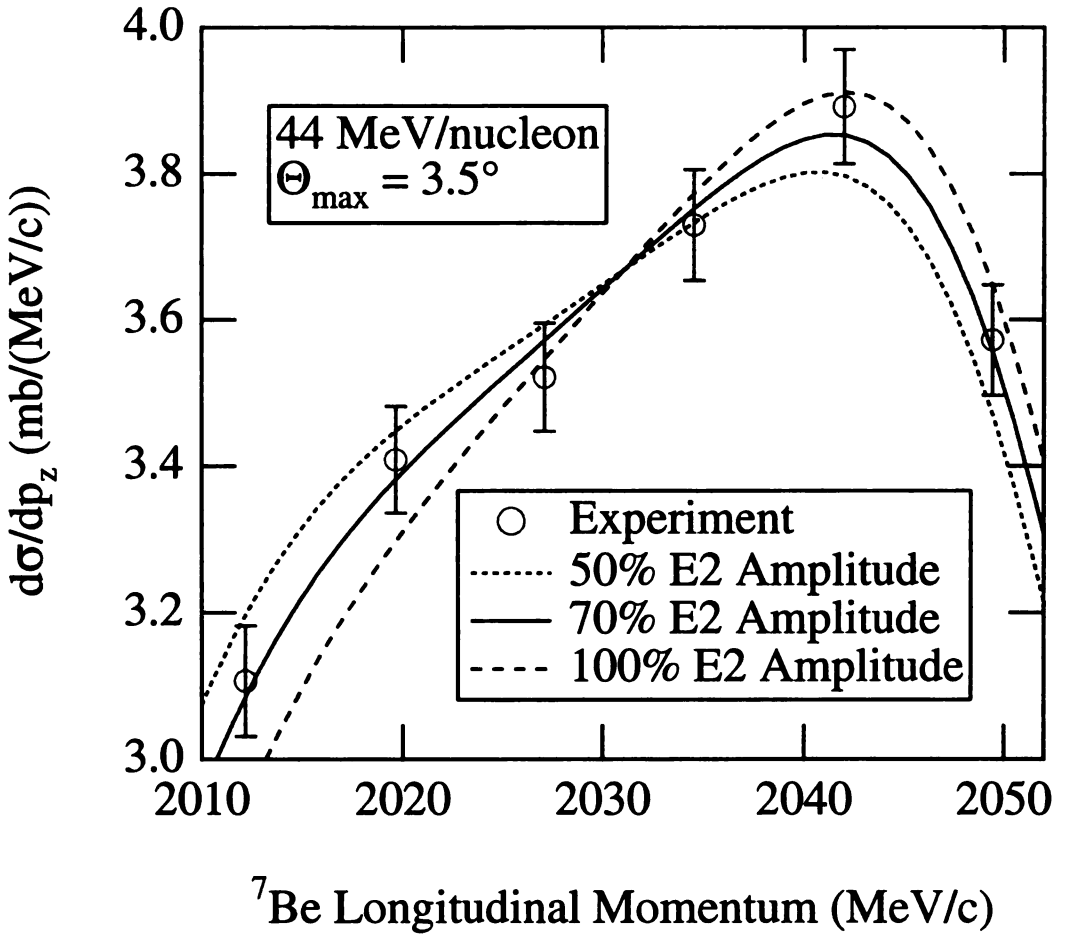

Figure 3.10: Central region of the 3.5° angle cut of the ^{7}Be longitudinal momentum distribution from the breakup of 44 MeV/nucleon ^{8}B on Pb. The curves are calculations performed with different E2 matrix elements, expressed in terms of the $E2$ amplitude of the model of [24], normalized to the center of the distribution.

Table 3.1: Integrated Coulomb dissociation cross sections

Target	Beam Energy (MeV/nucleon)	^{7}Be angle cut (°)	σ (mb)
Ag	44	1.5	61 (7)
Ag		2.0	97 (10)
Ag		2.5	140 (15)
Pb		1.5	68 (7)
Pb		2.4	156 (16)
Pb		3.5	252 (25)
Ag	81	1.25	67 (7)
Pb		1.5	130 (8)
Pb		2.0	201 (13)
Pb		2.5	266 (17)

that $S_{17}(0) = 19.1$ eV b, and that $S_{E2}/S_{E1} = 9.5\times10^{-4}$ at a relative energy of 0.6 MeV. The use of 1st-order perturbation theory is justified theoretically because of the small value of the electromagnetic strength parameter,

$$\chi_{i\to f}^{(E\lambda)} \simeq \frac{Z_t e\langle f||\mathcal{M}(E\lambda)||i\rangle}{\hbar v b^{\lambda}}, \tag{3.1}$$

which measures the number of photons exchanged in a transition [11]. The inverse dependence on the beam velocity v implies that for intermediate energy beams the strength parameter will be less than unity, guaranteeing that most processes are mediated by single photon exchange, and that 1st-order perturbation theory is a reasonable approximation.

We have also investigated the importance of higher-order electromagnetic effects and nuclear-induced breakup through continuum-discretized coupled channels (CDCC) calculations. In the CDCC approach [29], the breakup of ^{8}B is assumed to populate a selected set of spin-parity excitations with proton-^{7}Be relative energies up to some maximum value. This excitation energy range is subdivided into a number of intervals, or bins. For each such bin a representative square integrable wave function is constructed, a superposition of those proton-^{7}Be scattering states internal to the bin. These bin wave functions form an orthonormal basis for the expansion and coupled channels solution of the proton + ^{7}Be + target three-body wave function. This coupled channels solution is carried out here using the code FRESCO [30]. The subsequent evaluation of the fragment energy and angular distributions, from the CDCC bin-state inelastic amplitudes, is discussed in detail in ref. [31].

The parameter space used in the CDCC calculations is as follows. Partial waves up to $L_{max} = 15000$ and radii up to 1000 fm were used for the computation of the projectile-target relative motion wave functions. The wave functions for each bin and their coupling potentials were calculated using proton-^{7}Be separations up to 200 fm. Excitations up to a proton-^{7}Be relative energy of 10 MeV were considered. In these

calculations the ^{7}Be intrinsic spin is neglected, assuming that the core behaves as a spectator. The proton spin dependence is included, however, and all proton-^{7}Be relative motion excitations consistent with orbital angular momenta $\ell \leq 3$, i.e. relative motion states ℓ_j up to $f_{7/2}$, were included. The effects of the g-wave continuum are small and are neglected. The calculations use potential multipoles $\lambda \leq 2$ in the expansion of the proton- and ^{7}Be- target interactions. The real potential used to construct the wave functions for each bin was the same as that used to bind the ^{8}B ground state, a pure $p_{3/2}$ proton single-particle state. This proton-^{7}Be binding potential was taken from Esbensen and Bertsch [24], and was used for all spin-parity channels. The fragment-target nuclear interactions are also included; for the ^{7}Be-^{208}Pb system we take the (^{7}Li) interaction of Cook [32] and for the proton-^{208}Pb system the global nucleon optical potential of Becchetti and Greenlees [33].

3.3 Breakup Energy Spectrum

In contrast to the $E2$ component, the size of the $M1$ contribution to the cross section for Coulomb breakup can be determined from the measurement of the radiative capture cross section at the 0.64 MeV 1^+ resonance [8]. $M1$ transitions only play a role in Coulomb dissociation near this energy, and the magnitude of the contribution is obtained from the measured resonance parameters [34] and the calculated virtual photon spectrum [12]. The energy resolution of our exclusive measurement is too large and the contribution too small to allow us to clearly see this resonance, but it represents a few percent of the measured cross section.

Since the radiative capture reaction involves protons and ^{7}Be nuclei in their ground states, Coulomb breakup that yields excited ^{7}Be nuclei is not relevant to the inverse radiative capture rate. As our experimental setup did not include any provision for detecting γ rays, a correction for the yield to the $1/2^-$ excited state of ^{7}Be was made

on the basis of equation 41 of ref. [35], and the analysis of the data of ref. [36] found in ref. [37]. The size of this correction ranged from 1% at 200 keV to 9% at 2 MeV.

By placing a 1.77° cut on the reconstructed angle of the dissociated 83 MeV/nucleon ^{8}B projectiles, we have ensured that nuclear diffraction and absorption effects are small, and that the point-like projectile approximation employed in 1st-order perturbation theory is valid. Furthermore, by also excluding relative energies below 130 keV from our analysis, we minimized the role of $E2$ transitions and considered only relative energies where $E1$ was the dominant ($> 90\%$) contribution to the breakup. Fig. 3.11 shows the theoretical breakup energy spectrum calculated in 1st-order perturbation theory. The calculation was performed with the model of ref. [24] for the $E1$ and $E2$ components, scaling the $E2$ matrix elements by 0.7, while the $M1$ component was calculated as described above. As illustrated in Fig. 3.12, $E1$ transitions dominate the breakup cross section from 130 keV to 2 MeV except for a narrow range surrounding the 0.64 MeV 1^+ resonance. $E2$ transitions contribute significantly at relative energies under 130 keV, accounting for the sharp fall in the $E1$ fraction of the cross section at low relative energies.

To deduce the $E1$ strength at low relative energies, we carried out the following procedure. After fixing the $E2/E1$ ratio using the inclusive data, we convoluted the calculated $E1$, $E2$, and $M1$ cross sections with the energy-dependent experimental resolution, and then scaled the combined $E1 + E2$ cross section in order to minimize χ^2 for the measured differential cross section between 130 and 400 keV. Recent work [38] suggests that above 400 keV, nuclear structure uncertainties increase appreciably. The best-fit normalization factor of the $E1 + E2$ calculation for the data between 130 keV and 400 keV was $0.93\ ^{+0.05}_{-0.04}$, resulting in $S_{17}(0) = 17.8\ ^{+1.4}_{-1.2}$ eV b, with all sources of uncertainty added in quadrature. We extrapolated to zero energy using the prescription of Jennings *et al.* [38]. The quoted error (1σ) includes energy-dependent

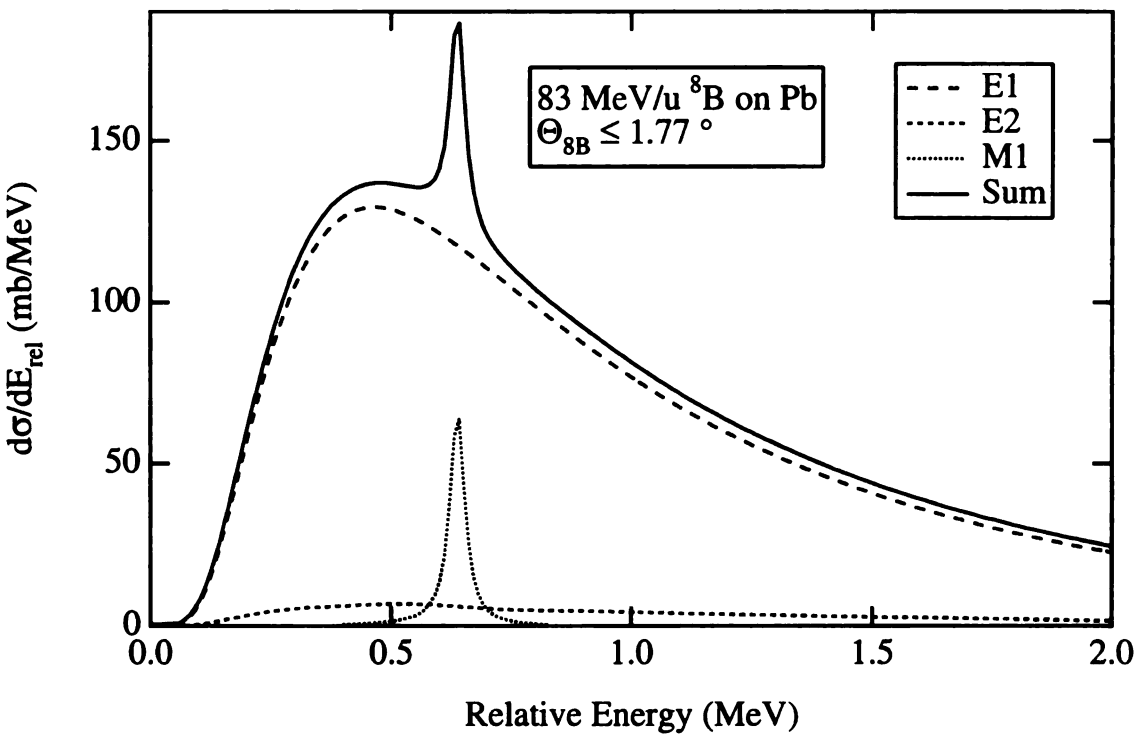

Figure 3.11: Contributions of $E1$, $E2$, and $M1$ transitions to the cross section for the Coulomb dissociation of 83 MeV/nucleon ^{8}B on Pb with ^{8}B scattering angles $\leq 1.77°$ in 1st-order perturbation theory. The $M1$ cross section is calculated by folding the $M1$ S factor measured in ref. [8] with the virtual photon spectrum. The $E1$ and $E2$ cross sections are calculated using the model of ref. [24], scaling the $E2$ matrix elements by the factor 0.7 required to reproduce the measured ^{7}Be longitudinal momentum distributions.

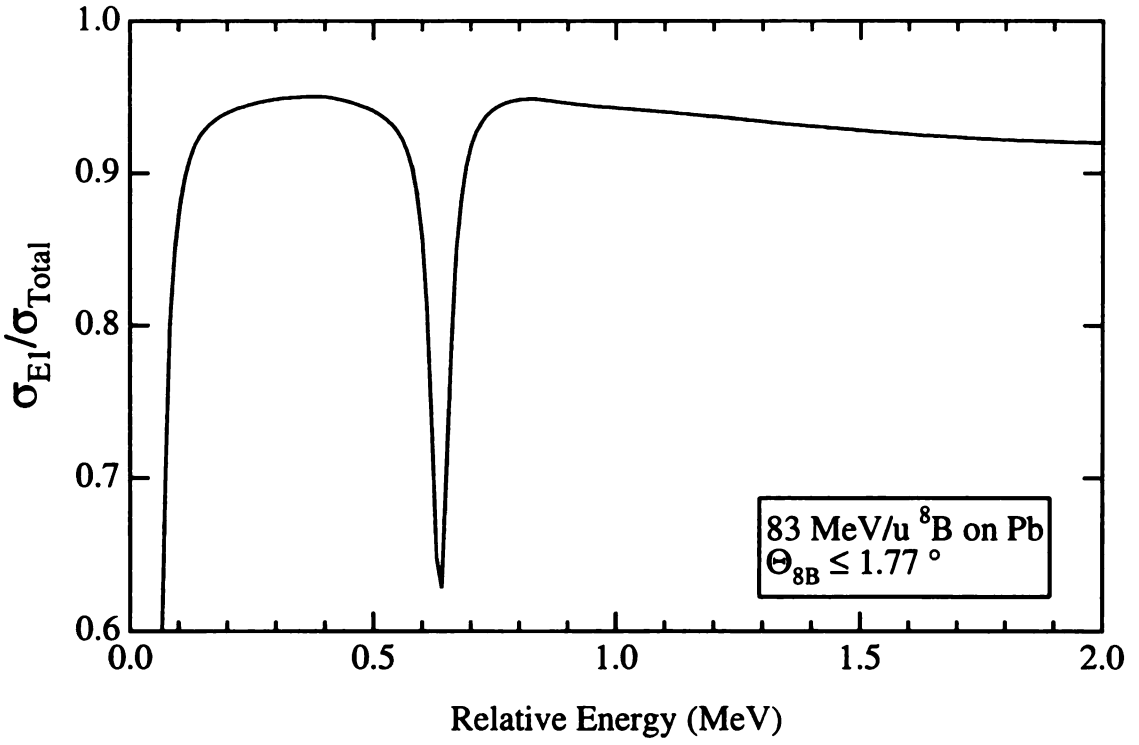

Figure 3.12: Fraction of the calculated cross section for the Coulomb dissociation of 83 MeV/nucleon ^{8}B on Pb with ^{8}B scattering angles $\leq 1.77°$ (b $\geq$ 30 fm) accounted for by $E1$ transitions in 1st-order perturbation theory. As the energy falls below 130 keV, $E2$ transitions become increasingly important.

contributions from statistics, momentum and angular acceptance, detector efficiency, and the ^{7}Be excited state yield correction, added in quadrature with systematic uncertainties from the beam intensity (1%), extrapolation to zero energy (1%), size of the $E2$ component (2.5%), target thickness (2.6%), and momentum calibration accuracy (4.2%).

We also analyzed the measured breakup cross section at higher relative energies, carrying out the same χ^2 minimization procedure for the data from 130 keV to 2 MeV. The data above 2 MeV were excluded from the fit because of a 3^+ resonance at 2.2 MeV that was not included in the theoretical calculation, and because the statistics there are poor. The best-fit normalization factor obtained for the data between 130 keV and 2 MeV with this procedure was $1.00\ ^{+0.02}_{-0.06}$. We assign a 5% theoretical extrapolation uncertainty for this energy range [38]. The result of the perturbation theory analysis of data from 130 keV to 2 MeV is $S_{17}(0) = 19.1\ ^{+1.5}_{-1.8}$ eV b. This result is consistent with the value extracted from the data up to 400 keV, implying that the simple potential model of ref. [24] describes the physics well even at large relative energies, within the uncertainties. Nevertheless, we prefer the value of $S_{17}(0)$ inferred from the data below 400 keV because of its relative insensitivity to the details of ^{8}B structure.

Fig. 3.13 shows the differential cross section measured in the exclusive experiment along with the results of our CDCC calculations, convoluted with the experimental resolution. The figure also includes the results of the best-fit 1st-order perturbation theory calculations for the two energy ranges described above using the model of ref. [24], with $E2$ matrix elements quenched as required to fit the inclusive data. The perturbation theory calculations include $M1$ transitions and also have been convoluted with the experimental energy resolution. The CDCC calculations employ a slightly simplified version of the structure model of ref. [24], and provide a means of gauging

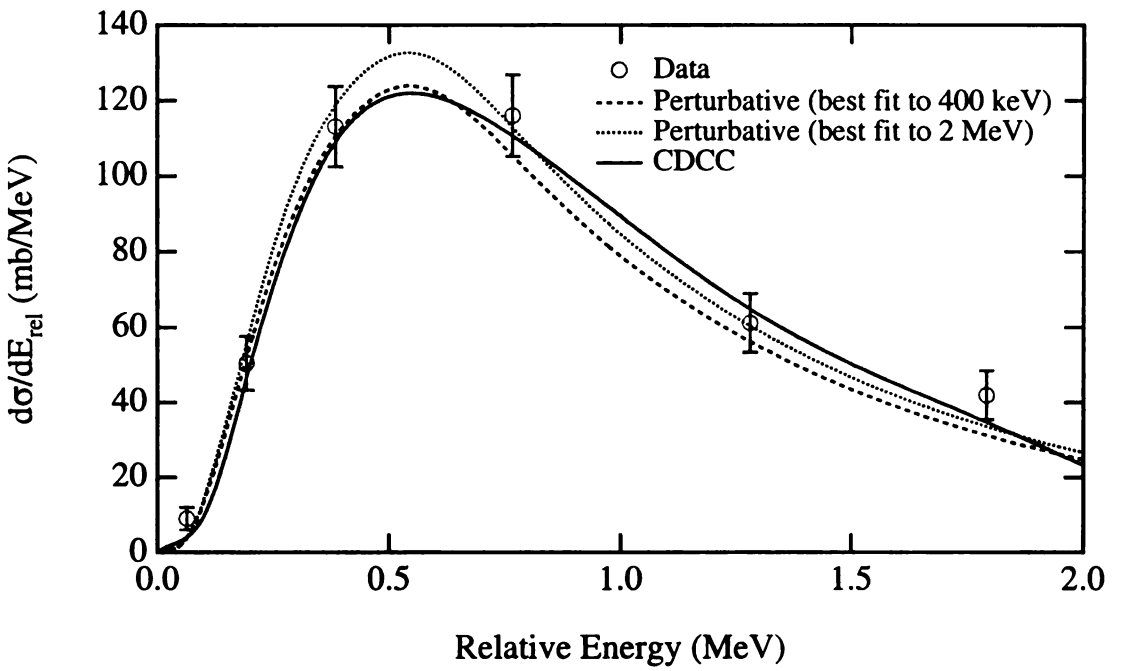

Figure 3.13: Measured differential cross section for the Coulomb dissociation of 83 MeV/nucleon ^{8}B on Pb with ^{8}B scattering angles $\leq 1.77°$. Only relative errors are shown. Also depicted are continuum-discretized coupled channels and two 1st-order perturbation theory calculations, convoluted with the experimental resolution. The point at 64 keV has been excluded from the fits because $E2$ transitions are dominant at this energy.

the importance of nuclear-induced breakup and higher-order electromagnetic effects; the $E1$ and $E2$ reduced transition probabilities predicted by the two structure models agree at the 1% level. These fully quantum mechanical CDCC calculations include both nuclear and Coulomb interactions, and have not been renormalized.

The two reaction models describe the data between 130 keV and 2 MeV equally well, implying that the theoretical uncertainties in the reaction mechanism are smaller than or comparable to the experimental uncertainties here. In large measure, this is due to the experimental conditions of the exclusive measurement. By limiting the angular acceptance as we did, we probed large impact parameters where the $E2$ and

nuclear contributions are small. These CDCC calculations indicate that nuclear-induced breakup is negligible at relative energies less than 400 keV. Higher-order electromagnetic effects are also smallest at the largest impact parameters [13, 24]. The fact that the zero energy S factors implicit in the CDCC calculation (18.9 eV b) and the best-fit 1st-order perturbation theory calculation for the data up to 2 MeV (19.1 eV b) agree within 1% gives confidence that 1st-order perturbation theory adequately describes the underlying physics of the breakup reaction under these experimental conditions, provided the $E2$ matrix elements are appropriately quenched.

Chapter 4

Discussion

The $E2$ strength deduced from the inclusive momentum distribution measurement is 10 to 100 times larger than the upper limits reported in other experimental studies [16, 36]. We studied an observable that directly probes $E1$-$E2$ interference, the asymmetry in the longitudinal momentum distribution. Our experimentally deduced value for the $E2/E1$ ratio is only slightly smaller than or in good agreement with recent theoretical calculations [24, 39, 40, 41, 42], and is consistent with the measurement of [43], although this group does not give a value for S_{E2}/S_{E1}. That the extracted experimental value should be somewhat smaller than the theoretical values is consistent with the idea that 1st-order perturbation theory overestimates the $E2$ contribution to the cross section [24]. Table 4.1 shows the $E2$ strength predictions given in several recent papers using potential models, microscopic cluster models, the shell model embedded in the continuum, and R-matrix theory, along with the results of this work. The concordance of these predictions of the $E2$ strength made on the basis of disparate theoretical methods and the result deduced from the measured longitudinal momentum distribution asymmetries imply that the $E2$ component must be accounted for in a proper theoretical description of the Coulomb breakup.

We interpret the required quenching of the $E2$ matrix elements in 1st-order per-

Table 4.1: Comparison of theoretical $E2$ strength predictions with present results

Author	Reference	Method	S_{E2}/S_{E1} (0.6 MeV)
Esbensen and Bertsch	[24]	potential model	9.5×10^{-4}
Typel *et al.*	[39]	potential model	8.0×10^{-4}
Bennaceur *et al.*	[40]	SMEC	7.72×10^{-4}
Descouvement and Baye	[41]	cluster model	6.2×10^{-4}
Barker	[42]	R-Matrix	8.7×10^{-4}
Davids *et al.*	this work	experiment	$4.7\ ^{+2.0}_{-1.3} \times 10^{-4}$

turbation theory as a manifestation of higher-order dynamical effects. For a fixed $E2$ strength, the predicted asymmetry of the longitudinal momentum distribution is diminished when higher-order effects are considered compared with 1st-order perturbation theory [24]. In dynamical calculations of the Coulomb dissociation of ^{8}B that include higher-order processes [24], the $E1$ strength is essentially unaltered, while the $E2$ strength is reduced with respect to 1st-order perturbation theory calculations. As such dynamical calculations are difficult and time-consuming, we have accounted for these effects by quenching the $E2$ matrix elements in the context of a 1st-order perturbation theory description of the reaction dynamics. The dynamical calculations include the same physics as do the CDCC calculations presented here. A comparison between the CDCC calculations and (1st-order) DWBA calculations using the same structure model indicates that the reduction in $E2$ strength caused by higher-order dynamical effects does not exhibit any significant relative energy dependence. Fig. 4.1 shows the result of this comparison. Hence the approach we have adopted, namely, scaling the $E2$ matrix elements by the same factor for all relative energies in 1st-order perturbation theory, is justified.

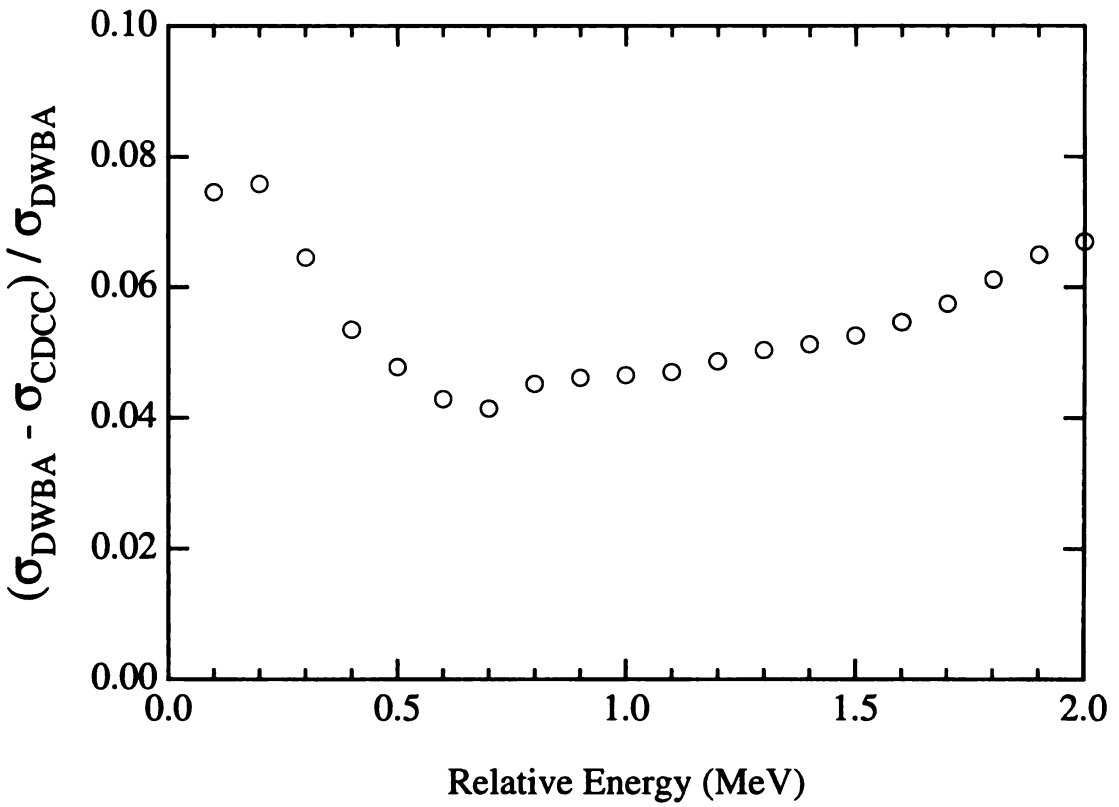

Figure 4.1: Difference between the cross section for Coulomb breakup of 83 MeV/nucleon ^{8}B on Pb for ^{8}B scattering angles of 1.77° and less predicted by DWBA (1st-order) and CDCC (all orders) calculations using the same structure model, expressed as a fraction of the DWBA prediction. Only Coulomb matrix elements were included in these calculations. No significant energy dependence of the higher-order electromagnetic effects is evident.

By measuring the Coulomb dissociation cross section at low relative energies and small scattering angles of the ^{8}B center-of-mass, we have ensured that the contribution of $E2$ transitions is small, and that nuclear diffraction effects are negligible. Using our inclusive measurement of ^{7}Be longitudinal momentum distributions to determine the relative contributions of the $E2$ and $E1$ components, we extracted the $E1$ strength at low relative energies from the exclusive measurement. The value of the astrophysical zero-energy S factor for the ^{7}Be(p,γ)^{8}B reaction we infer, 17.8 $^{+1.4}_{-1.2}$ eV b, is in good agreement with other recent measurements, and with the recommendation of a recent workshop on solar nuclear fusion cross sections [44]. Fig. 4.2 and table 4.2 show the results of recent radiative capture [8, 9], Coulomb breakup [15, 16], and asymptotic normalization coefficient [45] determinations of $S_{17}(0)$, along with the results of this work.

The concordance of our measurement and the other Coulomb breakup measurements conceals an underlying difference in interpretation. The analyses of references [15, 16] have treated the contributions of $E2$ transitions as negligible, while our data imply they are not. Since these experiments covered angular ranges larger than this measurement, they probed smaller impact parameters where $E2$ transitions are relatively more important. If $E2$ transitions are considered, 1st-order perturbation theory calculations imply that the astrophysical S factor inferred from the RIKEN Coulomb breakup measurement should be reduced by 4-15% [46], and that of the GSI measurement by 15-20%. Such a reduction would bring these measurements into even better agreement with the present work. If we were to analyze our measured Coulomb breakup cross section between 130 and 400 keV without considering $E2$ transitions, the extracted $E1$ strength would be 5% greater, and the inferred value of $S_{17}(0)$ would increase to 18.7 $\pm$ 1.3 eV b. The small $E2$ correction is the result of restricting the angular range covered in this experiment, making the $E2$ contribution

Table 4.2: Recent $S_{17}(0)$ determinations

Author	Reference	Method	$S_{17}(0)$ (eV b)
Filippone *et al.* reanalysis	[8, 9]	radiative capture	18.4 ± 2.2
Hammache *et al.*	[9]	radiative capture	18.5 ± 1.0
Kikuchi *et al.*	[15]	Coulomb breakup	18.9 ± 1.8
Iwasa *et al.*	[16]	Coulomb breakup	$20.6 \pm 1.0 \pm 1.0$
Azhari *et al.*	[45]	transfer reaction	17.3 ± 1.8
Davids *et al.*	this work	Coulomb breakup	$17.8\ ^{+1.4}_{-1.2}$

to the breakup cross section comparable in magnitude to the statistical uncertainty of the measurement.

It appears that the three techniques used to infer $S_{17}(0)$, direct radiative capture measurements, asymptotic normalization coefficient determinations, and Coulomb breakup, yield consistent results with different systematic uncertainties. In light of these facts, we take a weighted average of these measurements to obtain a recommended value. In this average, we include the radiative capture measurement of ref. [8], which was deemed the only reliable measurement at the 1997 workshop on solar nuclear fusion cross sections [44], and the recent measurement of ref. [9]. Here we use the reanalysis of the data of ref. [8] presented in ref. [9]. We also include the asymptotic normalization coefficient result [45] shown in table 4.2, and the present Coulomb breakup measurement. We do not include the other Coulomb breakup measurements [15, 16] in this average because we lack sufficient information to precisely correct for the $E2$ component neglected in the published analyses of these data. The weighted average we obtain is $\langle S_{17}(0) \rangle = 18.1 \pm 0.7$ eV b. This value of $S_{17}(0)$ implies a reduction of the predicted ^{8}B solar neutrino flux of about 5% from the value used

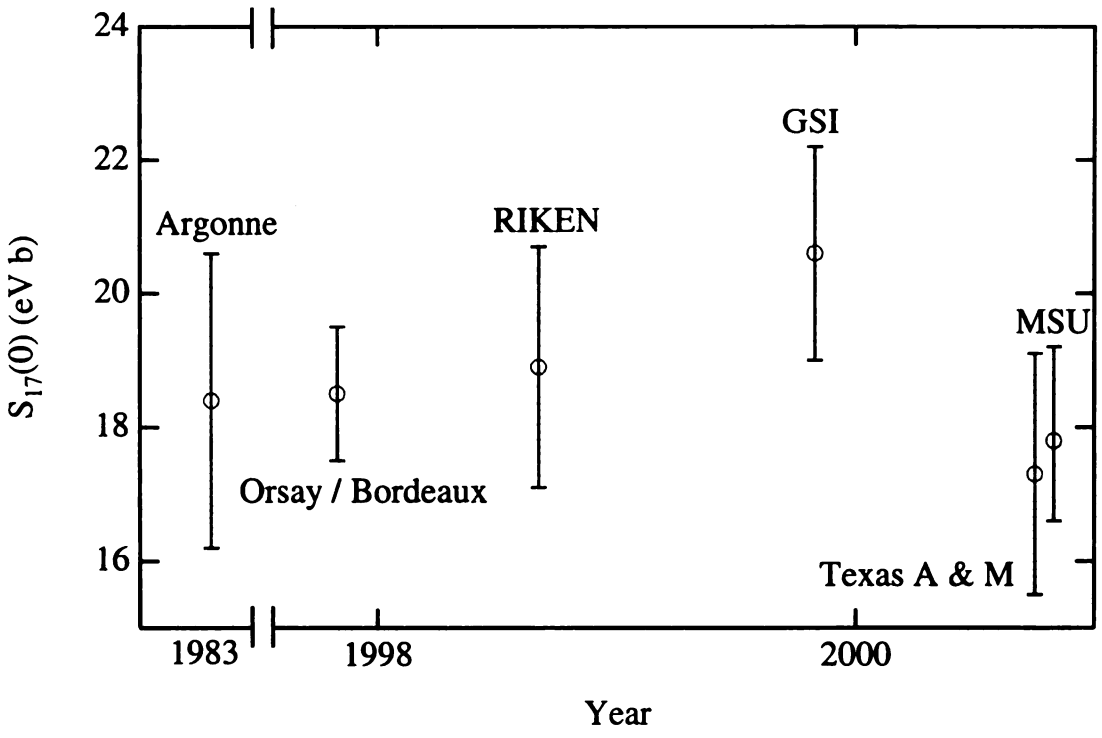

Figure 4.2: Inferred zero-energy astrophysical S factors for the ^{7}Be(p,γ)^{8}B reaction from recent direct and indirect measurements.

in ref. [1].

Chapter 5

Summary

In summary, we have carried out inclusive measurements of the Coulomb dissociation of ^{8}B on Pb and Ag targets at 44 and 81 MeV/nucleon. Using a high-resolution, large-acceptance magnetic spectrometer, we measured the distribution of longitudinal momenta of the emitted ^{7}Be fragments. The longitudinal momentum distributions reveal $E2$ strength in the Coulomb breakup in the form of an asymmetry produced by $E1$-$E2$ interference. By comparing the measured longitudinal momentum distributions with 1st-order perturbation theory calculations, we deduced the effective $E2$ contribution to the Coulomb breakup. Expressing our result as the ratio of $E2$ and $E1$ S factors at an energy where previous results have been compiled, we found $S_{E2}/S_{E1} = 4.7\ ^{+2.0}_{-1.3} \times 10^{-4}$ at $E_{rel} = 0.6$ MeV. This result is at least a factor of 10 larger than other experimental determinations, but in reasonably good agreement with theoretical predictions arrived at through several different methods.

In a separate experiment, we made an exclusive measurement of the Coulomb dissociation of 83 MeV/nucleon ^{8}B on a Pb target using a dipole magnet to separate the beam from the breakup fragments. Measuring the differential Coulomb breakup cross section at low relative energies and small ^{8}B scattering angles yielded the astrophysical S factor for the ^{7}Be$(p,\gamma)^8$B reaction with minimal complications from $E2$

transitions, higher-order electromagnetic effects, and nuclear-induced breakup. Interpreting this exclusive measurement in the context of a 1st-order perturbation theory description of the reaction dynamics and a single-particle potential model of ^{8}B structure, we obtained $S_{17}(0) = 17.8\ ^{+1.4}_{-1.2}$ eV b. We checked the validity of the perturbative approach through continuum-discretized coupled channels calculations that assume an essentially identical model of ^{8}B structure. The two reaction theories describe the data up to relative energies of 2 MeV equally well within the experimental uncertainties, implying that a slightly modified 1st-order perturbation theory is adequate for understanding the Coulomb breakup of ^{8}B at intermediate beam energies and small angles.

This measurement agrees well with other recent experimental determinations of $S_{17}(0)$, and shows that the uncertainties associated with the Coulomb breakup technique, unwanted multipolarities, higher-order electromagnetic effects, and nuclear-induced breakup, can be controlled well enough to obtain a precise value for the ^{7}Be(p,γ)^{8}B cross section. Direct radiative capture measurements, asymptotic normalization coefficient determinations, and Coulomb breakup measurements yield consistent results for $S_{17}(0)$, despite their different systematic uncertainties, giving confidence that this quantity is now well determined. We recommend a weighted average of measurements using these 3 different techniques, $\langle S_{17}(0) \rangle = 18.1 \pm 0.7$ eV b, for use in solar modeling. On the basis of this test case, we believe Coulomb breakup holds promise for indirectly measuring other radiative capture cross sections.

LIST OF REFERENCES

[1] J. N. Bahcall, S. Basu, and M. H. Pinsonneault, Phys. Lett. B **433**, 1 (1998).

[2] Y. Fukuda *et al.*, Phys. Rev. Lett. **82**, 2430 (1999).

[3] R. W. Kavanagh, Nucl. Phys. **15**, 411 (1960).

[4] P. D. Parker, Phys. Rev. **150**, 851 (1966).

[5] R. W. Kavanagh, T. A. Tombrello, J. M. Mosher, and D. R. Goosman, Bull. Am. Phys. Soc. **14**, 1209 (1969).

[6] F. J. Vaughn, R. A. Chalmers, D. Kohler, and L. F. Chase, Jr., Phys. Rev. C **2**, 1657 (1970).

[7] C. Wiezorek, H. Kräwinkel, R. Santo, and L. Wallek, Z. Phys. A **282**, 121 (1977).

[8] B. W. Filippone, A. J. Elwyn, C. N. Davids, and D. D. Koetke, Phys. Rev. Lett. **50**, 412 (1983); Phys. Rev. C **28**, 2222 (1983).

[9] F. Hammache *et al.*, Phys. Rev. Lett. **80**, 928 (1998).

[10] G. Baur, C. A. Bertulani, and H. Rebel, Nucl. Phys. A **458**, 188 (1986).

[11] A. Winther and K. Alder, Nucl. Phys. **A319**, 518 (1979).

[12] C. A. Bertulani and G. Baur, Phys. Rep. **163**, 299 (1988).

[13] G. Baur and H. Rebel, Annu. Rev. Nucl. Sci. **46**, 321 (1996).

[14] T. Motobayashi *et al.*, Phys. Rev. Lett. **73**, 2680 (1994).

[15] T. Kikuchi *et al.*, Eur. Phys. J. A **3**, 213 (1998).

[16] N. Iwasa *et al.*, Phys. Rev. Lett. **83**, 2910 (1999).

[17] B. M. Sherrill D. J. Morrissey, J. A. Nolen, N. Orr, and J. A. Winger, Nucl. Instrum. Methods B **70**, 298 (1992).

[18] J. A. Caggiano, Ph.D. thesis, Michigan State University, 1999.

[19] J. Yurkon, D. Bazin, W. Benenson, D. J. Morrissey, B. M. Sherrill, D. Swan, and R. Swanson, Nucl. Instrum. Methods A **422**, 291 (1999).

[20] M. Berz, K. Joh, J. A. Nolen, B.M. Sherrill, and A. F. Zeller, Phys. Rev. C **47**, 537 (1993).

[21] L. G. Atencio, J. F. Amann, R. L. Boudrie, amd C. L. Morris, Nucl. Instrum. Methods **187**, 381 (1981).

[22] K. Makino and M. Berz, Nucl. Instrum. Methods A **427**, 338 (1999).

[23] J. J. Kruse, Ph.D. thesis, Michigan State University, 1999.

[24] H. Esbensen and G. F. Bertsch Nucl. Phys. A **600**, 37 (1996).

[25] J. H. Kelley *et al.*, Phys. Rev. Lett. **77**, 5020 (1996).

[26] H. Esbensen, personal communication.

[27] H. Esbensen and G. F. Bertsch, Phys. Lett. B **359**, 13 (1995).

[28] B. Davids *et al.*, Phys. Rev. Lett. **81**, 2209 (1998).

[29] M. Kamimura *et al.*, Prog. Theor. Phys. Suppl. **89**, 1 (1986); N. Austern *et al.*, Phys. Rep. **154**, 125 (1987).

[30] I. J. Thompson, Comp. Phys. Rep. **7**, 167 (1988).

[31] J. A. Tostevin, F. M. Nunes, and I. J. Thompson, submitted for publication.

[32] J. Cook, Nucl. Phys. **A388**, 153 (1982).

[33] F. D. Becchetti and G. W. Greenlees, Phys. Rev. **182**, 1190 (1969).

[34] F. Ajzenberg-Selove, Nucl. Phys. A **490**, 1 (1988).

[35] C. A. Bertulani, Phys. Rev. C **49**, 2688 (1994).

[36] T. Kikuchi *et al.*, Phys. Lett. B **391**, 261 (1997).

[37] A. Mengoni, T. Motobayashi, and T. Otsuka, in *Nuclei in the Cosmos V*, edited by N. Prantzos and S. Harissopulos (Editions Frontiéres, Paris, 1998).

[38] B. K. Jennings, S. Karataglidas, and T. D. Shoppa, Phys. Rev. C **58**, 3711 (1998).

[39] S. Typel, H. H. Wolter, and G. Baur, Nucl. Phys. A **613**, 147 (1997).

[40] K. Bennaceur *et al.*, Nucl. Phys. A **651**, 289 (1999).

[41] P. Descouvement and D. Baye, Phys. Rev. C **60**, 015803 (1999).

[42] F. Barker, Nucl. Phys. A **660**, 249 (1999).

[43] V. Guimarães *et al.*, Phys. Rev. Lett. **84**, 1862 (2000).

[44] E. G. Adelberger *et al.*, Rev. Mod. Phys. **70**, 1265 (1998).

[45] A. Azhari *et al.*, Phys. Rev. Lett. **82**, 3960 (1999); Phys. Rev. C **60**, 055803 (1999); Phys. Rev. C, submitted for publication.

[46] T. Motobayashi, personal communication.